JGR Solid Earth

RESEARCH ARTICLE
10.1029/2023JB027502

Path and Slip Dependent Behavior of Shallow Subduction Shear Zones During Fluid Overpressure

Benjamin D. Belzer[1] and **Melodie E. French**[1]

[1]Department of Earth, Environmental and Planetary Sciences, Rice University, Houston, TX, USA

Key Points:

- Effective stress path and rock composition control effects of high pore fluid pressure on fault constitutive behavior
- Stress path effects on frictional behavior are more pronounced in simulated chlorite gouge than celadonite gouge due to differences in microstructure
- Chlorite-rich faults stabilize with increasing displacement at high pore fluid pressure and slow slip speeds

Supporting Information:

Supporting Information may be found in the online version of this article.

Correspondence to:

B. D. Belzer,
bbelzer@rice.edu

Citation:

Belzer, B. D., & French, M. E. (2024). Path and slip dependent behavior of shallow subduction shear zones during fluid overpressure. *Journal of Geophysical Research: Solid Earth*, *129*, e2023JB027502. https://doi.org/10.1029/2023JB027502

Received 20 JULY 2023
Accepted 29 MAR 2024

Author Contributions:

Conceptualization: Benjamin D. Belzer
Data curation: Benjamin D. Belzer
Formal analysis: Benjamin D. Belzer
Funding acquisition: Melodie E. French
Investigation: Benjamin D. Belzer
Methodology: Benjamin D. Belzer
Resources: Melodie E. French
Supervision: Melodie E. French
Visualization: Benjamin D. Belzer
Writing – original draft: Benjamin D. Belzer, Melodie E. French
Writing – review & editing: Melodie E. French

Abstract Elevated pore fluid pressure is proposed to contribute to slow earthquakes along shallow subduction plate boundaries. However, the processes that create high fluid pressure, disequilibrium compaction and dehydration reactions, lead to different effective stress paths in fault rocks. These paths are predicted by granular mechanics frameworks to lead to different strengths and deformation modes, yet granular mechanics do not predict their effects on fault stability. To evaluate the role of fluid overpressure on shallow megathrust strength and slip behavior, we conducted triaxial shear experiments on chlorite and celadonite rich gouge layers. Experiments were conducted at constant temperature (130 and 100°C), confining pressure (130 and 140 MPa), and pore fluid pressures (between 10 and 120 MPa). Fluid overpressure due to disequilibrium compaction was simulated by increasing confining and pore fluid pressure synchronously without exceeding the target effective pressure, whereas overpressure due to dehydration reactions was simulated by first loading the sample to a target isotropic effective pressure and then increasing pore fluid pressure to reduce the effective pressure. We find that the effects of fluid pressure and stress path on the mechanical behavior of the chlorite and celadonite gouges can generally be described using the critical state soil mechanics (CSSM) framework. However, path effects are more pronounced and persist to greater displacements in chlorite because its microstructure is more influenced by stress path. Due to its effects on microstructure, the stress path also imparts greater control on the rate-dependence of chlorite strength, which is not predicted by CSSM.

Plain Language Summary High pore fluid pressure has been linked to complex slip modes along subduction plate boundary faults, such as low frequency earthquakes and slow slip. However, the role that pressurized fluids play in controlling these slip modes remains unclear. Along shallow subduction faults (<10 km), the source of pore fluid overpressure transitions with increasing depth from disequilibrium compaction of sediments to fluid release due to dehydration reactions like the smectite to illite transition. Using deformation experiments, we studied how different stress paths simulating these two processes affect the mechanical, frictional, and microstructural properties of shallow subduction fault rock at high fluid pressure.

1. Introduction

Increases in pore fluid pressure have long been cited to decrease the effective normal stress on faults and facilitate deformation at low shear stress (King Hubbert & Rubey, 1959). This has been proposed to cause transient or long-term slip along unfavorably oriented faults, including high-angle reverse shear zones, low-angle overthrusts and detachments, and the San Andreas Fault in California (e.g., Byerlee, 1990; Sibson et al., 1988; Sleep & Blanpied, 1992), as well as induced seismicity during wastewater injection (e.g., Ellsworth, 2013). On the basis of geodetic and seismic observations over the past two decades (e.g., Kodaira et al., 2004; Shelly et al., 2006), elevated pore fluid pressure has also been invoked as the cause of different slip modes (e.g., nonvolcanic tremor, low-frequency earthquakes, and slow slip) that have profound significance for earthquake hazards in subduction zones. However, the potential role of fluids along subduction thrust faults is debated as the indication that fault zones are overpressured and therefore weak does not necessarily account for the intermediate strain rates and episodic nature of these phenomena (Beeler et al., 2013).

In addition, recent laboratory and numerical studies indicate that elevated pore fluid pressure can both stabilize and destabilize fault slip through evolving porosity, permeability, and strength during sliding (e.g., Bedford et al., 2021; Faulkner et al., 2018; den Hartog & Spiers, 2013; Scuderi & Collettini, 2016; Scuderi et al., 2017; Xing et al., 2019). This presents further difficulty not only in determining what role(s) fluids play in the mechanics of slow slip events (SSE), but in constraining the seismic potential of any fault zone in which fluid

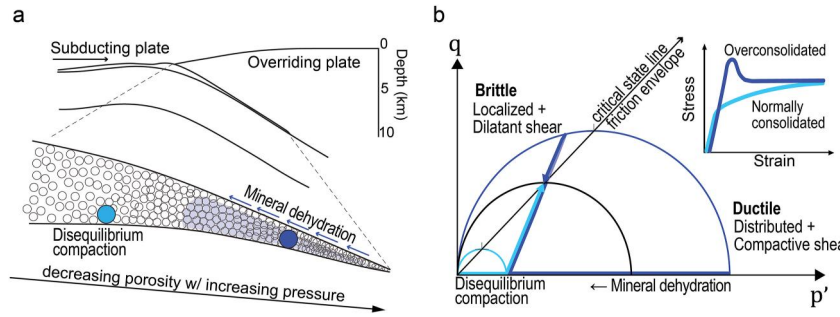

Figure 1. Conceptual diagram of (a) two processes that create pore fluid overpressure in the shallow region of subduction plate boundaries, disequilibrium compaction and dehydration reactions, and (b) the effective stress paths and deformation modes that granular materials are predicted to experience as a result. (a) Generalized view of the shallow subduction zone interface, adapted from Bilek and Lay (1999), where granular materials experience decreasing porosity and increasing rigidity as they subduct. (b) Schematic of the effective stress paths associated with disequilibrium compaction (light blue) and dehydration (dark blue), in which granular materials become normally consolidated and overconsolidated, respectively. The critical state line (CSL) defines the stress configuration at which the material behaves in a perfectly plastic manner and is equivalent to the steady-state friction envelope. The ellipses represent yield curves based on the modified Cam-clay model, which increase in size with decreasing porosity and lead to different modes of deformation depending on whether the stress path intersects the yield curve to the right or left of the CSL. To reach critical state, the yield curves expand when shear occurs in the ductile field (right of the CSL) or contract when shear occurs in the brittle field (left of the CSL). As such, materials that are normally consolidated compact and strain-harden in the ductile field, while those that are overconsolidated dilate and strain-weaken in the brittle field before reaching critical state, as illustrated in the upper right plot.

pressure is high. Determining how pore fluids affect not just the strength of faults, but their slip characteristics, thus remains an important goal in improving earthquake models and providing more accurate seismic hazard assessment.

There are different causes of fluid pressurization, particularly within the subduction zone forearc. Studies on fluid flow, pore pressure, and metamorphism in the forearc region indicate that multiple processes create pressurized pore fluid (Figure 1a), yet it is unclear if the cause imparts any control on fault deformation and slip behaviors. In some cases, elevated fluid pressures are generated when shallow seawater-rich sediments on the subducting plate undergo disequilibrium compaction during rapid burial and tectonic loading (Neuzil, 1995). This process, in which sediment compaction outpaces the rate of pore pressure diffusion, acts as the dominant source of fluid pressurization within the outermost forearc (Saffer & Tobin, 2011). In contrast, deeper regions of high pore fluid pressure develop when metamorphic dehydration reactions introduce new fluids, which then migrate updip (Hacker et al., 2003; Peacock, 2009).

Here, we examine how the endmember paths of pore fluid pressurization due to disequilibrium compaction and dehydration reactions influence the mechanical and microstructural properties of shallow subduction fault rock. In particular, we evaluate how path-dependent evolution of porosity and microstructure influences the strength evolution and frictional rate-dependence. To do so, we conducted two suites of triaxial shear experiments, one on synthetic chlorite gouge and another using phyllosilicate-rich fault rock from the Rodeo Cove thrust zone in California. The strength and its rate-dependence were measured at the same effective pressures but different consolidation states. By comparing the two materials, we evaluate the role that compositional heterogeneity and resulting microstructure play in controlling the path dependence of deformation.

2. Critical State Soil Mechanics Framework

The critical state concept of soil mechanics is a useful framework for describing how the strength and porosity of deforming granular materials evolve (Wood, 1990). Although the concept of critical state originates from soil mechanics, it has been applied to a number of geologic topics including elasto-plastic deformation in sedimentary basins and accretionary complexes (e.g., Karig & Morgan, 1994) and the shearing of fault gouge (e.g., Karner et al., 2005; Marone et al., 1990). Within this framework, the porosity of granular material develops according to its effective stress and consolidation history, eventually reaching constant porosity and a critical state strength. Thus, diverging effective stress paths give rise to different strength and structural evolutions.

Stress paths associated with evolving pore fluid pressure can be visualized in two-dimensional stress space of differential stress (σ_d or q) and effective mean stress ($\sigma_{m'}$ or p') (Figure 1b). In this space, the size of the material yield envelope, which is often described using a modified Cam-clay model developed by Roscoe and Burland (1968), increases with decreasing porosity. Yield envelopes are intersected at their apex by the critical state line which separates the stress space into brittle and ductile modes of deformation. During deformation, the strength evolves toward the critical state line, which is equivalent to the steady-state frictional strength. At lower effective mean stresses where the yield envelope is above the critical state line, once the stress state reaches the yield envelope, it contracts and deformation is dilatant, localized, and strain weakening (brittle) until the strength reaches the critical state line. In contrast, at higher effective mean stresses where the yield envelope is below the critical state line, once the stress state reaches the yield envelope, it expands and deformation is compactive, distributed, and strain-hardening (ductile) until the strength reaches the critical state line. The porosity and size of the yield envelope are determined by the effective stress history of the granular material, with higher effective stresses resulting in lower porosities and larger yield envelopes.

Different sources of pore fluids lead to different pore pressure and effective stress histories, which control deformation processes in sediment and porous sedimentary rocks through their consolidation state. The consolidation state of granular material is often described by the overconsolidation ratio (OCR), defined as the ratio of the highest effective stress the material previously experienced to its current effective stress (e.g., Jones, 1994; Kitajima et al., 2012). Sediments are overconsolidated if OCR >1 and normally consolidated if OCR = 1. The term underconsolidated is sometimes used to describe the situation in which fluid pressure does not dissipate with an applied load; however, by definition, this is a normally consolidated effective stress state. Due to its porosity reduction, an overconsolidated granular material has a larger yield envelope than a normally consolidated material being deformed at the same effective pressure (Figure 1b). Whereas triaxial shear of a normally consolidated material will always occur in the ductile, compactive field, deformation of overconsolidated material may either occur within the ductile, compactive field or brittle, dilatant field (Figure 1b). When overconsolidation results in ductile, compactive deformation it is called "lightly overconsolidated" and when it results in brittle, dilatant behavior it is termed "heavily overconsolidated." Although the exact OCR for which a material behaves `heavily overconsolidated' varies, a rule of thumb is that OCR > 4–6 leads to heavily overconsolidated behavior.

Thus, critical state theory predicts that when secondary generation of fluids (e.g., through dehydration) results in pore fluid overpressure, granular material will become overconsolidated due to a reduction in effective stress and may exhibit dilatant, localized, and brittle shear if it is heavily overconsolidated (Jones, 1994) (Figure 1b). In contrast, if high pore fluid pressures originate early in the deformation history (e.g., through disequilibrium compaction), the granular material will be normally consolidated and exhibit compaction and distributed, ductile shear. However, constitutive relations that are used to model fault slip, such as rate-and-state friction, rarely incorporate the effects of increasing pore fluid pressure other than as a decrease in effective stress. Yet, applied concepts of critical state theory indicate that evolving fluid pressure modifies the stress path of granular fault rock (e.g., fault gouge), which may impact their consolidation state, microstructure, and rheological behavior if they retain memory of past stress. This implies that the origin of overpressure within the deformation history of fault zones may be important in controlling the relationship between pore fluid pressure and fault slip behavior.

3. Materials and Methods

3.1. Samples

Two simulated fault gouges were prepared from (a) an Fe-rich chlorite schist obtained from Ward's Natural Science and (b) foliated cataclasite collected from the Rodeo Cove thrust in California (Figure 2a). The chlorite schist is from the same sample whose temperature and rate-dependent strength was reported in Belzer and French (2022). It has the chemical formula $(Mg_{1.331}Fe^{2+}_{3.282}Al_{1.329}Na_{0.016}Ti_{0.008}Ca_{0.004})(Si_{2.665}Al_{1.335})O_{10}(OH,O)_8$ which is close to chamosite, the Fe^{2+}-rich endmember of the chlorite group. The simulated chlorite gouge contains >97% chlorite with minor amounts of ilmenite and monazite. The foliated cataclasite was sampled from and compositionally represents the dense, distributed network of phyllosilicate-rich shear bands that concentrated slip in the Rodeo Cove thrust zone, described by Meneghini and Moore (2007). Wavelength dispersive spectroscopy (WDS) data, electron dispersive spectroscopy (EDS), and quantitative area analysis of back-scattered

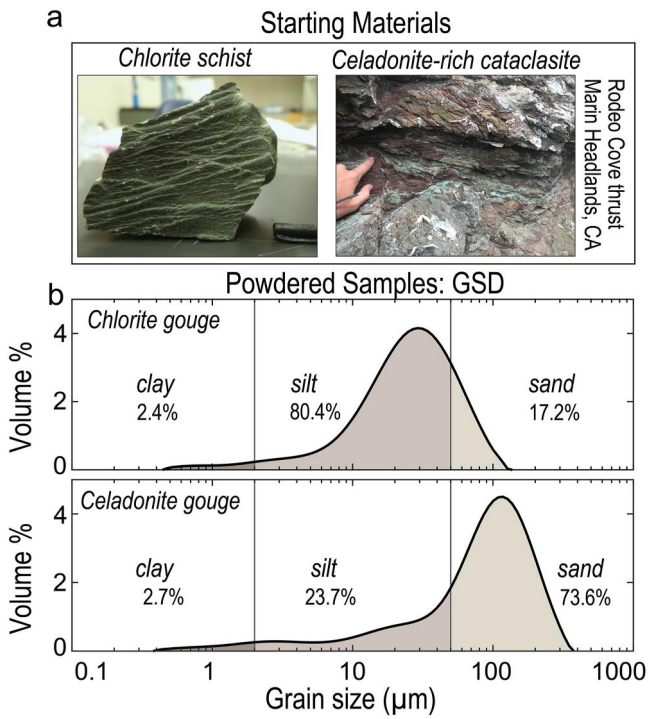

Figure 2. (a) Intact samples of commercially obtained chlorite schist and natural celadonite-rich cataclasite collected from the Rodeo Cove thrust zone in the Marin Headlands, California. (b) Grain size distributions (GSD) of samples after they were powdered to simulate fault gouges, with noted percentages of sand-sized particles (>50 μm), silt particles (2–50 μm), and clay particles (<2 μm).

electron (BSE) images indicate that over 90% of the foliated cataclasite consists of celadonite, an Fe- and K-rich diotachedral mica, with minor amounts of iron-oxyhydroxides, calcite, titanite, chlorite, and spinel.

The chlorite schist and foliated cataclasite were crushed and sieved to <75 and <125 μm, respectively. Grain size distributions (GSD) were measured using a Mastersizer 2000 laser particle size analyzer and Calgon (sodium hexametaphosphate) as a dispersing agent (Abdulkarim et al., 2021). Crushed samples of chlorite schist and foliated cataclasite (hereon referred to as chlorite and celadonite gouge, respectively) show unimodal and asymmetrical grain size distributions with respective peaks at 30 and 118 μm and tails toward the fine-grained fraction (Figure 2b). Silt-sized grains (2–50 μm in diameter) make up 80% of the chlorite gouge, whereas 74% of the celadonite gouge is comprised of sand-sized grains (>50 μm). Clay-sized grains (<2 μm) make up less than 3% of the particles in both the samples.

3.2. Experimental Procedure

We measured the strength and constitutive behavior of the simulated gouges at different effective pressures and consolidation states. Chlorite and celadonite gouge layers were sheared in the triaxial shear configuration between cylindrical steel forcing blocks 25.4 mm in diameter with a sawcut 35° to the core axis (Figure 3). The sawcut surfaces are grooved to promote shear within the gouge layer and a porous frit 13 mm in diameter sits in a recess of the surface to distribute pore fluid. For each experiment, 10 g of chlorite or 4 g of celadonite were mixed with distilled water to make a paste, which was spread on one of the blocks using a loading jig to create a uniform layer and then sandwiched with the other block. The sample was then placed between a top and bottom platen and jacketed with three polyolefin sleeves. The gouge layers of chlorite and celadonite had initial thicknesses of 5 and 2.5 mm, respectively.

Experiments were conducted in a servo-controlled triaxial deformation apparatus (Figure 3). The apparatus uses a hydraulic pressure system to control differential load, confining pressure (σ_3), and pore fluid pressure (P_f). Silicon oil is used as the confining fluid and distilled water is used as pore fluid. Confining and pore fluid pressures are measured with an accuracy of 0.01 MPa and linear voltage differential transformers (LVDTs) record displacement of the confining and pore pressure intensifier pistons. Volume change in the sample is calculated from the displacement of the pore pressure intensifier piston. Differential load is measured with an internal load cell and converted to differential stress (σ_d) by dividing by the cross-sectional area of the forcing blocks. Vertical shortening of the sample is calculated from the displacement of the axial piston, which is measured with an external LVDT and corrected for the elastic distortion of the apparatus using a calibrated stiffness of 2.5×10^8 N/m. The pressure vessel is externally heated and temperature (T) is maintained to within 5°C of the setpoint using an internal thermocouple.

The shear stress, τ, normal stress, σ_n, and effective normal stress, $\sigma_n' = \sigma_n - P_f$, along the saw cut are calculated from measurements of differential stress, confining pressure, and pore fluid pressure using standard procedures (e.g., Chester, 1994; Tembe et al., 2010). We corrected differential stress for both the strength of the polyolefin jackets and the change in sawcut surface area with slip (Belzer & French, 2022). The frictional strength of the gouge is reported as τ/σ_n', where near steady-state values are the friction coefficient, μ, assuming zero cohesion which is common for studies of gouge friction. Displacement along the sawcut is determined from measurements of axial displacement corrected for apparatus distortion.

To evaluate the roles of elevated pore fluid pressure and effective stress path on fault strength and stability, we conducted experiments under different consolidation paths and pore fluid pressures. We conducted hydrothermal shear experiments on chlorite and celadonite gouges at constant temperature (130 and 100°C), confining pressure (130 and 140 MPa), and pore fluid pressures (between 10 and 120 MPa) (Table 1). Some samples were first preconsolidated under isotropic stress conditions prior to shearing at elevated fluid pressure. We use the definition

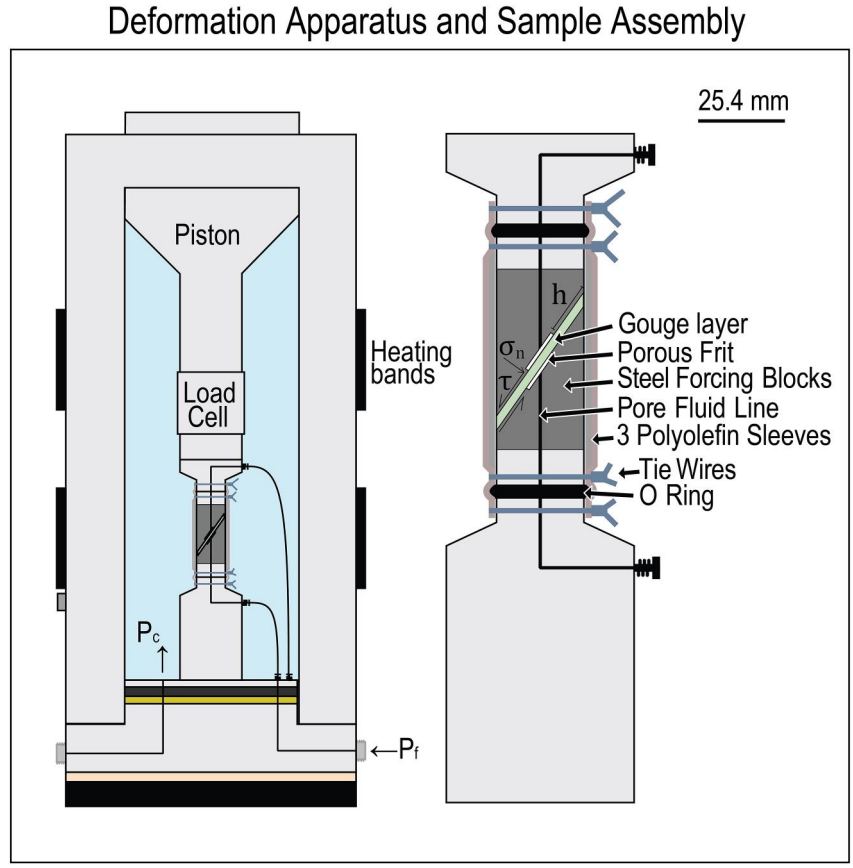

Figure 3. Schematic of the triaxial deformation apparatus and saw-cut configuration used in our study. P_c indicates confining pressure (i.e., σ_3) and P_f indicates pore fluid pressure. Shear stress and normal stress in the gouge layer are indicated by τ and σ_n, and h shows the maximum diffusion length for pore fluid along the tip of the forcing blocks to reach the porous frit.

of overconsolidation ratio (OCR) as the ratio of maximum effective pressure ($\sigma_3' = \sigma_3 - P_f$) imposed during preconsolidation (σ_{3o}') to the effective pressure at the onset of triaxial loading (σ_3'), that is, OCR = σ_{3o}'/σ_3' (Jones, 1994; Kitajima et al., 2012). Thus, OCR = 1 is a normal consolidation path and OCR >1 is an overconsolidation path (Figure 1b). Our experiments were conducted at OCRs of one and seven to target normally

Table 1
Deformation Experiments and Conditions

Experiment ID	T (°C)	σ_3 (MPa)	P_f (MPa)	σ_3' (MPa)	OCR	V (μm/s)	Initial s.d. (mm)	Total s.d. (mm)	Final gouge thickness (mm)
CHL7	130	130	10	120	1	1|0.1|0.01|0.001|0.01|0.1|1|1|10|1|10	2.5	7.5	2.1
CHL3	130	130	60	70	1	1|0.1|0.01|0.001|1|1|10|1|0.1	2.5	6.4	2.7
CHL9	130	130	120	10	1	1|0.1|0.01|0.001|0.01|0.1|1|1|10|1|10	1.2	6.3	3.4
CHL18	130	130	120	10	1	1|0.1|0.01|0.001|0.01|0.1|1|1|10|1|10	4.9	10.3	3.3
CHL4	130	130	120	10	7	1|0.1|0.01|0.001|0.01	1.1	2.8	3.8
CHL5	130	130	120	10	7	1|0.1|0.01|0.001|0.01|0.1|1|1|10|1|10	1.1	6.5	3.5
CHL19	130	130	120	10	7	1|0.1|0.01|0.001|0.01|0.1|1|1|10|1|10	4.9	10.3	3.1
RCC6	100	140	60	80	1	1|0.1|0.01|0.001|0.01|0.1|1|1|10|1|10	2.9	8.0	1.4
RCC3	100	140	120	20	1	1|0.1|0.01|0.001|0.01|0.1|1|1|10|1|10	3.1	8.2	1.6
RCC5	100	140	120	20	7	1|0.1|0.01|0.001|0.01|0.1|1|1|10|1|10	3.2	8.3	1.5

Note. Constant confining pressure (σ_3), pore fluid pressure (P_f), and effective pressure (σ_3') are reported during triaxial shear for each experiment. Shear displacements (s.d.) are listed for when the first velocity step was imposed (initial s.d.) and at the end of the deformation experiment (total s.d.).

consolidated and heavily overconsolidated behavior. We evaluate the role of effective stress path by conducting the shear experiments at the same effective pressure (10 or 20 MPa), but different OCRs. To evaluate the role of pore fluid pressure independently, two additional chlorite gouge samples and one celadonite gouge sample were sheared at OCR = 1 and lower pore fluid pressure (higher effective pressure).

Experiments on normally consolidated samples were conducted by ramping the confining pressure and pore fluid pressure synchronously at 1 MPa/min without exceeding the target effective confining pressure. After reaching the target effective pressure, the temperature was increased to 100 or 130°C over a duration of ∼5 hr while the confining pressure and pore fluid pressure were held constant. The temperature and pressure conditions were then held constant for 15 to 20 more hours prior to triaxial loading. In comparison, overconsolidated samples were preconsolidated at an effective confining pressure 7 times the target condition (OCR = 7). After ramping the confining and fluid pressure at 1 MPa/min to the target consolidation conditions, the temperature was increased over ∼5 hr and the sample was allowed to consolidate for at least 15 hr. Subsequently, the pore fluid pressure was increased at 1 MPa/min to reduce the effective pressure and conditions were held for at least 4 hr prior to initiating shear, which is sufficient to all fluid pressure equilibration based on our calculation of fluid diffusion time scales below.

Triaxial shear experiments were carried out with an initial shear velocity of 1 μm/s until samples yielded and showed constant strength or strain hardening behavior. We then imposed rate steps between 0.001 and 10 μm/s every 0.5–0.6 mm of shear displacement except during the slowest velocity which was held for 0.2–0.3 mm displacement. The total duration of each shear experiment was between 80 and 140 hr. For experiments on normally consolidated and overconsolidated chlorite gouge at 120 MPa pore fluid pressure, we varied the amount of shear displacement between 1 and 5.5 mm before initiating the rate steps to evaluate how strain influences rate-dependence. Most samples of chlorite and celadonite gouge were then sheared to total displacements between 6.3 and 10.3 mm. One experiment on overconsolidated chlorite gouge (CHL4), however, ended after only 2.8 mm of shear displacement, as the sample displayed an anomalously large stress drop (>50% reduction in frictional strength) after the fourth rate step.

We quantify the steady state rate-dependence of the strength using the rate- and state-friction framework (Dieterich, 1978; Ruina, 1983). The steady state rate-dependence is given by $\frac{d\mu_{ss}}{d \ln V}$, often referred to as "a–b," where μ_{ss} is the steady state friction coefficient and V is shear velocity. We determined the rate-dependence from our data using the RSF3000 code developed by Skarbek and Savage (2019), treating sample stiffness as a fitting parameter. We individually model frictional responses across 300 μm of slip before and after the rate steps using the aging law (Dieterich, 1979):

$$\frac{d\theta}{dt} = 1 - \frac{V\theta}{D_c}$$

where θ is a time-dependent state variable, V is the sliding velocity, and D_c is the critical slip distance required to restore a population of grain contacts. In experiments that did not reach a steady-state frictional strength, the data were first detrended to account for strain hardening or softening using RSF3000.

During shear deformation, the pore fluid pressure is held constant and at nearly drained conditions using the servo-controlled pore fluid intensifier piston. Since the pore fluid pressure is measured and controlled externally, we calculate the maximum shear velocities at which saturated layers of chlorite and celadonite remain sufficiently drained during the rate-steps. This allows us to evaluate if steady state rate-dependencies arise from intrinsic frictional processes or the effects of undrained or partially drained conditions (e.g., Faulkner et al., 2018). The time required for pore pressure to diffuse through the gouge layer is:

$$t = \frac{h^2 \beta \eta}{2k}$$

where h is the diffusion length, β is the compressibility of the fault gouge ($\sim 10^{-10}$ Pa^{-1} based on Wibberley (2002)), η is the viscosity of the pore fluid, and k is the permeability of the gouge. We use the viscosity of water at room temperature (0.001 Pa s), which conservatively provides an upper bound for the diffusion time as water

viscosity is expected to decrease at elevated temperature and pressure (Watson et al., 1980). To evaluate the longest flow path for pore fluid to diffuse into or out of the sample, we treat the diffusion length, h, as the distance between the furthest tip of the sawcut and the edge of the porous frit along the sawcut surface (0.015 m) (Figure 3). We measured the permeabilities of the chlorite and celadonite layers prior to shear, using the flow-through method and Darcy's law. Measurements were conducted at room temperature, effective pressures of 10 and 70 MPa, and a pore fluid pressure gradient of 1 MPa. The permeability measurements on chlorite gouge range from 1.2×10^{-17} m^2 to 5.9×10^{-17} m^2 and on celadonite gouge from 1.1×10^{-18} m^2 to 1.9×10^{-18} m^2. We assume a reduction in permeability during shear deformation by a factor of 20, as reported in similar samples by Ikari et al. (2009). Given these parameters, we calculate that the maximum diffusion time is ~18 s in the chlorite gouge and ~208 s in the celadonite gouge. By assuming that the samples must be fully drained over 150 μm of slip to determine the steady-state rate-dependence, which is one half the slip interval used to model slip behavior, we calculate that drained conditions are maintained up to slip rates of 8.1 μm/s for chlorite and 0.7 μm/s for the celadonite. Thus, the chlorite gouge is fully drained at all but the highest velocity (10 μm/s) and the celadonite gouge is fully drained at velocities up to 0.1 μm/s.

To evaluate path-dependent volume changes in the gouge layers, we measured changes in pore volume in the overconsolidated chlorite and celadonite gouge during isotropic loading and in all samples during triaxial shearing at relatively fast velocities (1 and 10 μm/s). During isotropic loading, pore volume reduction was measured in overconsolidated chlorite gouge (CHL19) with increasing effective pressure from 10 to 70 MPa and in overconsolidated celadonite gouge (RCC5) from 35 to 140 MPa. Based on their compaction trends with increasing effective pressure, we also estimated the amount of volume reduction in the other samples during isotropic loading, except sample CHL7 which was normally consolidated at higher effective pressure (120 MPa) than sample CHL19. During triaxial shearing, we measured pore volume changes leading up to the first velocity step (i.e., during the initial ~1–5 mm of slip) and during the last ~2.5 mm of slip. Volume changes during the slow velocity steps (0.001–0.1 μm/s), which in duration lasted from several hours to a few days, could not be measured due to noise in the pore pressure intensifier LVDT signal, caused by changing environmental factors in the laboratory (e.g., room temperature).

At high effective pressure (130 and 140 MPa), pore volume change was also measured in the chlorite and celadonite gouge as they were heated from room temperature to 130°C or 100°C, respectively, and while elevated temperature was subsequently held constant for 10–15 hr (Supporting Information S1, Figure S1). Thermal compaction and time-dependent compaction at elevated temperature was observed in both samples, where pore volume decreased by 0.35 cm^3 in the chlorite gouge and 0.2 cm^3 in the celadonite gouge. Although we were only able to resolve temperature-dependent compaction during these two tests (in which pore fluid pressure was held constant at only 1 or 2 MPa during the heating stage and had sufficiently equilibrated in the sample), we assume that prior to triaxial loading, each of the other chlorite and celadonite gouges also compacted by 0.35 cm^3 or 0.2 cm^3 due to increasing temperature. This assumption is supported by previous laboratory experiments that show that between 25 and 150 MPa effective pressure, water-saturated phyllosilicate-rich fault gouge undergoes consistent volume reduction with increasing temperature from 20 to 150°C (Faulkner & Rutter, 2003). Nevertheless, it is worth noting that pore volume reduction during heating may have slightly varied in some of our other samples, which could impact some of our results and interpretations.

Changes in the thickness of the gouge layers were not measured while at pressure or during shearing. However, two samples (CHL3 and RCC6) were unloaded after the isotropic loading stage, allowing us to directly measure their preconsolidated thickness before restarting the experiment. We measured that the chlorite gouge compacted from 5 to 3.1 mm at 70 MPa effective pressure and the celadonite gouge compacted from 2.5 to 2.1 mm at 80 MPa. Additionally, we measured the final thickness of the gouge layers after samples were sheared, unloaded, and removed from the apparatus (Table 1).

3.3. Microscopy

We examined the microstructures that developed in the chlorite and celadonite gouge using polarized and back-scattered electron (BSE) microscopy. Back-scattered electron images were collected at an accelerating voltage of 15 kV and a working distance of 11 mm using a JEOL 6500F Scanning Electron Microscope at Rice University. We report the microstructures that formed at almost all conditions in our study, except for the structures in

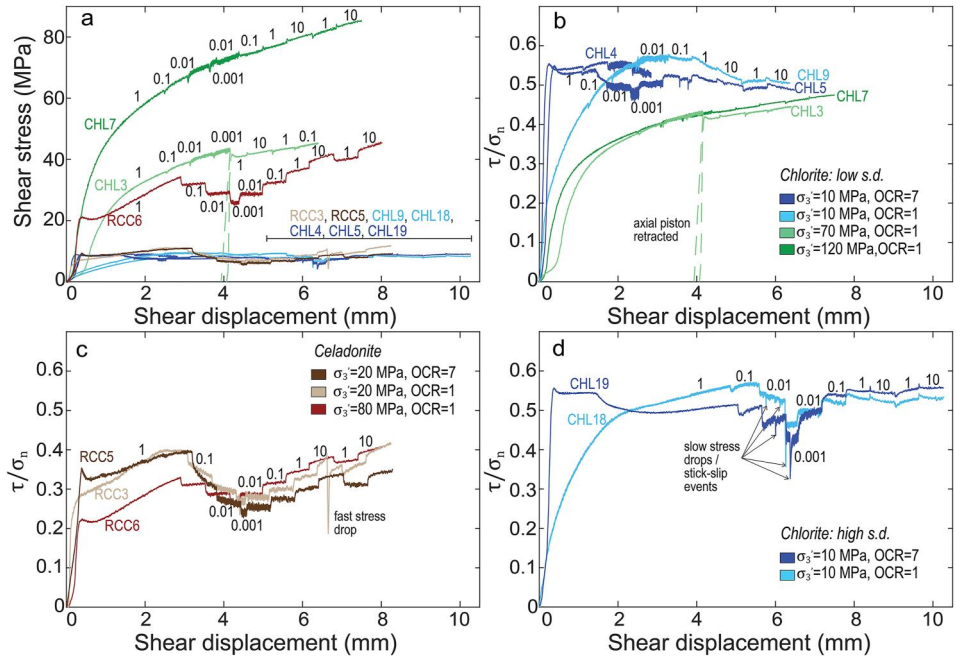

Figure 4. Mechanical data for sheared chlorite and celadonite gouge layers. (a) Shear stress with increasing shear displacement for all rate-stepping tests with numbers in black indicating visible rate steps (μm/s), (b) Chlorite frictional strength, expressed as τ/σ_n', with increasing displacement. Experiments conducted at OCR = 1 and different effective pressure from 10 to 120 MPa are shown in light blue (10 MPa), light green (70 MPa) and dark green (120 MPa). Experiments conducted at different overconsolidation ratios at 10 MPa effective pressure are shown in light blue (OCR = 1) and dark blue (OCR = 7). Data for CHL4 are plotted just before the sample displayed a fast stress drop from τ/σ_n' = 0.51 to 0.23, after which the experiment ended. Sample CHL3 was unloaded and reloaded at ~4 mm of displacement. (c) Celadonite frictional strength with increasing shear displacement. Experiments conducted at OCR = 1 and different effective pressures are shown in light brown (20 MPa) and red (80 MPa). Experiments conducted at 20 MPa effective pressure and different OCRs are shown in light brown (OCR = 1) and dark brown (OCR = 7), (d) Chlorite frictional strength when sheared to greater displacements at 10 MPa effective pressure (OCR = 1, light blue and OCR = 7, dark blue). Slow stress drops and stick-slip events as labeled in (d) occur in both chlorite and celadonite gouge sheared at high pore fluid pressure and slow shearing velocities (Supporting Information S1, Figure S2).

celadonite gouge sheared at 80 MPa effective pressure as we were unsuccessful in preserving that sample after the experiment.

4. Results

4.1. Strength

The shear strengths of the chlorite and celadonite gouge samples increase with confining pressure and have a second order dependence on slip rate across all experimental conditions, indicating frictional deformation (Figure 4a). The frictional strength of the chlorite (μ = 0.4 to 0.6) is higher than that of the celadonite (μ = 0.2 to 0.4) at similar effective pressure and shear displacements (Figures 4b and 4c). In both gouge samples, the evolution of strength with strain depends on consolidation state and effective stress in ways that are generally consistent with critical state theory. For both, differences in the strength of samples deformed at different consolidation states occur at relatively low displacements and they evolve to become similar at higher displacements.

Normally consolidated chlorites strengthen nonlinearly for 2–3 mm of displacement nearly from the onset of triaxial loading (Figure 4b). Although normally consolidated chlorite samples sheared at 10 MPa effective pressure (120 MPa pore pressure) reach steady state strength by ~5.5–6.5 mm displacement, samples deformed at 70 and 120 MPa effective pressure exhibit strain-hardening behavior throughout the experiment. These samples never reach the steady-state frictional strength of the low effective stress sample. In contrast, overconsolidated chlorite samples display linear elastic behavior prior to yield and then a sharp initial peak strength between 0.2 and

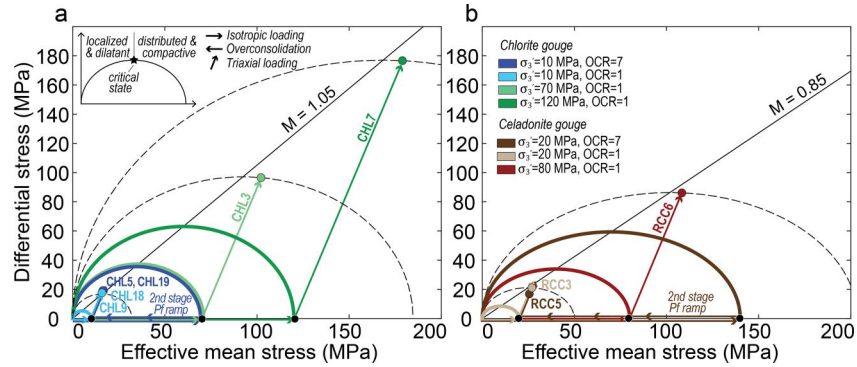

Figure 5. Schematic summary of experimental stress paths shown in q–p' space for gouge layers of (a) chlorite and (b) celadonite. Arrowed lines show the normal consolidation and overconsolidation paths during isotropic loading (horizontal) and triaxial loading stages (diagonal) for each experiment. Black points on the horizontal axis (p' = 0) mark preconsolidation stresses, while colored points show achieved stress states at the onset of the last velocity steps (1→10 μm/s or 1→0.1 μm/s). Elliptical curves indicate yield surfaces according to the modified Cam-clay model. Solid curves in color show yield curves produced through preconsolidation, while dashed curves show their predicted expansion and contraction during shear for normally consolidated and overconsolidated samples, respectively. Critical state lines are plotted as straight black lines and calculated using friction coefficients for (a) chlorite (μ = 0.5) and (b) celadonite (μ = 0.4) assuming zero cohesion. Predicted deformation modes and volume changes are indicated in the inset of (a).

0.4 mm of displacement that leads to strain-weakening. Subsequently, shearing in two of the overconsolidated chlorite gouges (CHL5 and CHL19) occurs at constant strength until 1.4 mm displacement, followed by a second stage of strain-weakening behavior that gradually leads to near-steady state deformation (Figures 4b and 4d). This differs from sample CHL4 which also shows an overconsolidation peak but subsequently shows a transition from slightly strain-hardening to slightly strain-weakening behavior, prior to sudden failure of the sample. Otherwise, the strengths of both the normally and overconsolidated chlorites sheared at the same effective pressure (10 MPa) tend to be nearly identical by approximately 6 mm of displacement (e.g., CHL5, CHL9, CHL18, and CHL19).

The strengths of normally and overconsolidated celadonite gouges evolve to be similar by ∼1 mm displacement (Figure 4c), which is lower displacement than required for the chlorite gouge. At 20 MPa effective pressure, the normally consolidated celadonite gouge strengthens monotonically during the initial 1 mm of shear displacement, whereas the overconsolidated sample exhibits a sharp peak strength, similar to the differences seen in the chlorite samples. Like chlorite, the frictional strength of celadonite gouge is initially lower at higher effective pressure (80 MPa) and strain-hardens toward similar values with increasing displacement. Unlike chlorite, however, normally consolidated celadonite sheared at 80 MPa effective pressure also exhibits a small peak in strength before strain-hardening throughout most of the experiment. At 20 MPa effective pressure, celadonite layers display strain-weakening behavior between ∼3 and 4.5 mm of displacement, coeval with stepwise velocity changes from 1 to 0.001 μm/s, regardless of consolidation state. Subsequently, the celadonite layers deformed at 20 MPa tend to exhibit steady-state behavior during shear at low velocities (0.001–0.1 μm/s) and strain-hardening behavior at faster velocities (1–10 μm/s), except for RCC5 which shows steady-state behavior at 1 μm/s following the second-to last velocity step.

Occasionally, the chlorite and celadonite gouges exhibit stress drops when sheared at high pore fluid pressure. Slow stress drops that last ∼1–13 min in duration occur during slow shearing velocities (0.001–0.01 μm/s) in both overconsolidated and normally consolidated gouge and are associated, in most cases, with stick-slip behavior where their frictional strength recovers (Supporting Information S1, Figure S2). In contrast, when sheared at the fastest slip rate (10 μm/s), normally consolidated and overpressured celadonite gouge (RCC3) displays a significant stress drop which lasts <1 s and which is preceded by transient strain-hardening behavior (Figure 4c).

We use the CSSM approach to summarize the path dependent strengths of the chlorite and celadonite gouge layers and their respective yield envelopes during the different experiments (Figure 5). We plot elliptical yield curves that represent the modified Cam-clay model developed by Roscoe and Burland (1968), as shown in Figure 1b. Each yield curve has an elliptical shape defined by:

$$q^2 + M^2\left(p' - p'_o\right)p' = 0$$

where q is differential stress, p' is effective mean stress, p_b is the preconsolidation stress, and M is the slope of the critical state line. We determine M using its relationship to the angle of internal friction (ϕ) based on Equation 54 from Roscoe and Burland (1968), where:

$$M = \frac{6\sin\phi}{3 - \sin\phi}$$

The angle of internal friction is determined from the friction coefficients ($\mu = \tan\phi$) of the chlorite and celadonite gouges, respectively. For the chlorite gouge, μ is taken to be 0.5 based on its average residual friction values at 10 MPa effective pressure, and for the celadonite gouge, μ is taken to be 0.4 based on its strain-hardening behavior generally observed at high displacements and τ/σ_n' values < 0.4. This produces slopes of $M = 1.05$ for the chlorite sample and $M = 0.85$ for the celadonite sample. For each experiment, we plot two yield curves: one at the onset of triaxial loading (i.e., before shear) and another near the end of the shear experiment at the end of the last 1 μm/s velocity step. These diagrams demonstrate that, to a first-order, the mechanical data are consistent with the CSSM framework. Differences in the mechanical behavior of normally and overconsolidated samples at low effective pressure can be understood as occurring because of deformation within the ductile and brittle fields of the respective yield envelopes. In addition, strain-hardening trends in chlorite at high effective pressure can be understood as ductile deformation that has not yet reached critical state. However, we find that the yield envelopes based on the modified Cam-clay model overestimate the peak strengths we measure for overconsolidated chlorite and celadonite gouges.

4.2. Volumetric Deformation

During triaxial shear, trends in the pore volume changes in the chlorite and celadonite gouges are also generally consistent with predictions of critical state theory. Normal consolidation correlates to compaction during shear, whereas overconsolidation correlates to dilation or lower compaction rates (Figure 6). As displacement increases, volume changes become small to negligible in all samples. Also, changes in pore volume tend to correlate with changes in the strength of the gouge layers.

During isotropic loading, pore volume in sample CHL19 decreases 1 cm^3 from 10 to 70 MPa effective pressure (Figure 6a), indicating the initial difference in volume between overconsolidated chlorite gouge (CHL4, CHL5, CHL19) and normally consolidated chlorite gouge (CHL9, CHL18) sheared at 10 MPa effective pressure. During heating, each of the chlorite layers are also assumed to compact by 0.35 cm^3 (Supporting Information S1, Figure S1). Subsequently, normally consolidated chlorite gouges compact during triaxial loading, whereas overconsolidated chlorite layers either dilate or show nearly constant pore volume with slip (Figures 6a and 6b). Normally consolidated chlorite gouges compact the most when sheared at the lowest effective pressure (10 MPa), although there is no consistent trend with the normally consolidated samples sheared at higher effective pressures (Figure 6b). In addition, the rate of pore volume reduction decreases with increasing shear displacement in the normally consolidated chlorite gouges. This trend continues at higher displacements as observed during the final series of rate steps between 1 and 10 μm/s (Figure 6c). In contrast, overconsolidated chlorite layers tend to dilate during most of shear deformation. However, we observe there are two periods of shear deformation where sample CHL19 displays slight compaction with displacement. First, at approximately 0.5 mm of shear displacement, the pore volume response in CHL19 temporarily transitions from dilation to slight compaction with shear (Figure 6d). We note this transition in pore volume response coincides with a transition from strain-weakening behavior (following peak strength) to steady-state frictional sliding, and that after ~1.4 mm displacement, dilation in sample CHL19 resumes during the second stage of strain-weakening behavior. Secondly, we observe that the pore volume response in CHL19 transitions again from slight dilation to slight compaction after 8.8 mm of shear displacement (Figure 6c).

The celadonite gouges all compact during the initial ~3 mm of shear displacement regardless of consolidation state (Figure 6b). However, triaxial loading of the overconsolidated celadonite initially coincides with dilation leading up to its peak strength, followed by compaction (Figures 6a and 6d). Like chlorite, the normally consolidated celadonite gouge sheared at the lowest effective pressure (20 MPa) compacts the most, followed by

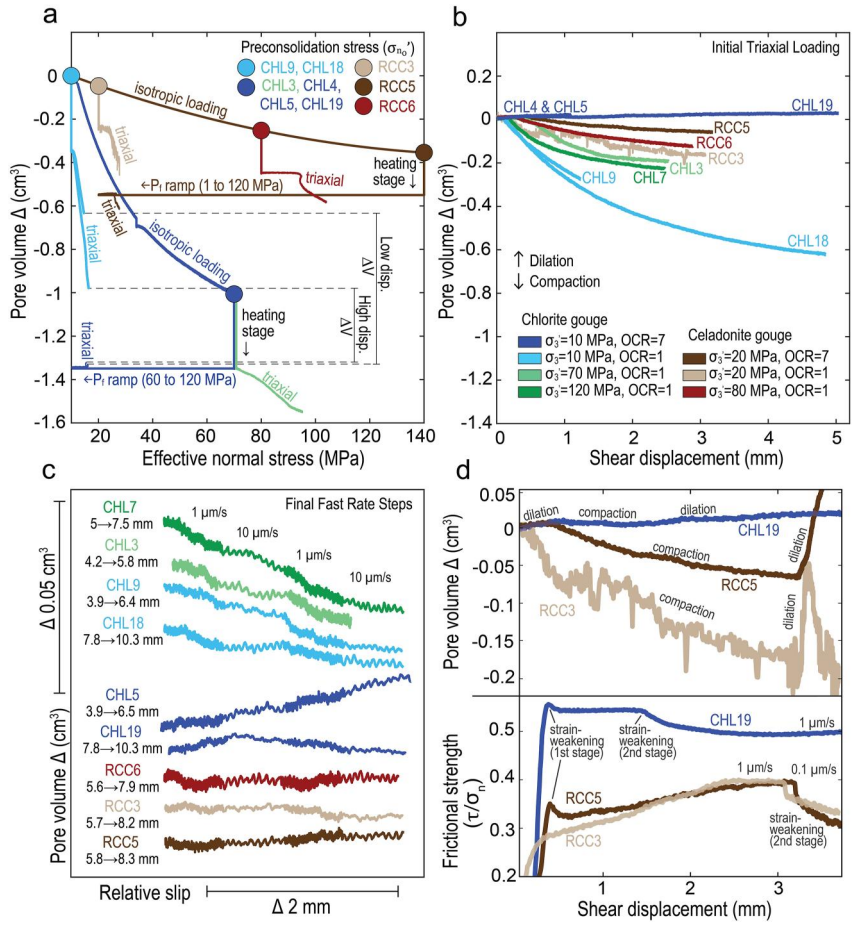

Figure 6. Summary of absolute pore volume changes in normally consolidated and overconsolidated chlorite and celadonite gouge layers during isotropic and triaxial loading. Note that the chlorite samples have an initial thickness (and volume) approximately two times that of the celadonite samples. (a) Pore volume change versus effective normal stress in samples during isotropic loading, heating, and triaxial loading until the first velocity step. Volume change is set to zero at 10 MPa and 25°C, which are the initial preconsolidation conditions for CHL9 and CHL18. Compaction curves during isotropic loading are shown for overconsolidated chlorite (CHL19: blue) and celadonite gouge (RCC5: brown) and used to estimate changes in pore volume in other samples during preconsolidation, as denoted by the colored circles. Sample CHL7, which was normally consolidated at higher effective normal stress (120 MPa) than CHL19, is not shown. After preconsolidation, further decreases in pore volume during heating are shown by the colored vertical lines, where $\Delta V = -0.35$ cm^3 in chlorite gouge heated to 130°C and $\Delta V = -0.20$ cm^3 in celadonite gouge heated to 100°C. During increases in pore fluid pressure for the overconsolidated tests (OCR = 7), pore volume is assumed constant while effective normal stress decreases from 70 to 10 MPa for chlorite gouge (blue horizontal line) and from 140 to 20 MPa for the celadonite gouge. Dashed horizontal lines indicate differences in pore volume between the normally consolidated and overconsolidated chlorite samples at ~1 mm (low disp. ΔV) and ~5 mm of shear displacement (high disp. ΔV), coinciding with the start of the first velocity step (1→0.1 μm/s). (b) Changes in pore volume with shear displacement in the chlorite and celadonite layers during initial triaxial loading at 1 μm/s, up to ~1–5 mm of shear displacement. (c) Relative pore volume changes with shear displacement in the chlorite and celadonite samples at greater displacements, measured during the last four velocity steps between 1 and 10 μm/s. (d) Evolution of pore volume (upper plot) and frictional strength (bottom) with shear displacement in samples CHL19, RCC5, and RCC3.

the normally consolidated sample at higher effective pressure (80 MPa). However, the overconsolidated celadonite sheared at 20 MPa also shows a net reduction in pore volume during initial triaxial shearing, in contrast with the overconsolidated chlorite gouge which shows a net increase in pore volume. At ~3 mm displacement, pore volume change in the overconsolidated sample transitions from compaction to dilation (Figure 6d), closely following the first velocity step from 1 to 0.1 μm/s and a shift from strain-hardening to strain-weakening behavior. Generally, all celadonite samples exhibit negligible pore volume change at displacements greater than 5.6 mm (Figure 6c).

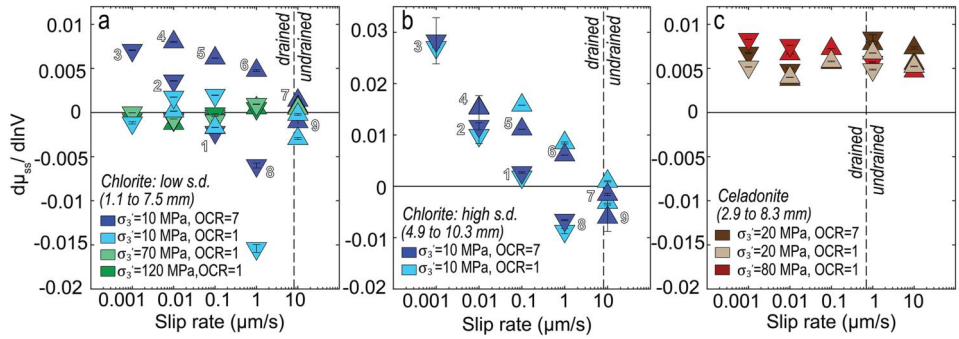

Figure 7. (a) Steady-state rate-dependence of chlorite strength at low shear displacements (s.d. 1.1–7.5 mm) at different effective pressures and OCR = 1 (10 MPa: light blue, 70 MPa: light green, 120 MPa: dark green) and at different OCRs and 10 MPa effective pressure (OCR = 1: light blue, OCR = 7: dark blue). (b) Rate-dependence of chlorite strength at high displacements (s.d. 4.9–10.3 mm) at different consolidation states. Note the larger scale of the vertical axis. (c) Rate-dependence of celadonite strength at different effective pressures and OCR = 1 (20 MPa: light brown, 80 MPa: red) and at different consolidation states and 20 MPa effective pressure (OCR = 1: light brown, OCR = 7: dark brown). Triangles are plotted at the shearing velocity that the sample is stepped to during a velocity step, whereby upward triangles indicate stepwise increases in velocity and downward triangles indicate stepwise decreases in velocity. The order of the velocity steps is notated by the white numbers in (a) and (b) for reference. Vertical dashed lines at 8.1 μm/s for chlorite and 0.7 μm/s for celadonite indicate the maximum slip rates that ensure they are fully drained. Thus, velocity up-steps to the right of the line or velocity down-steps left of the line may have been undrained.

4.3. Rate-Dependent Friction

The chlorite and celadonite gouge layers show different patterns in the second order dependence of strength on rate. The rate-dependence of chlorite strength varies with effective stress, consolidation path, and shear displacement (strain) (Figure 7). Normally consolidated chlorite gouges deformed at the highest effective pressures (70 and 120 MPa) show a consistent transition from slightly rate-weakening (a–b = −0.001) at slow velocities (0.001–0.1 μm/s) to slightly rate-strengthening (a-b = 0.001) at fast velocities (1–10 μm/s) (Figure 7a). At shear displacements less than 4.9 mm and low effective pressure (10 MPa), normally consolidated chlorite gouge has similar behavior at the lowest velocity, but slightly rate-strengthens (a–b = 0.002) between 0.01 and 0.1 μm/s and rate weakens (a–b = -0.015 to −0.002) between 1 and 10 μm/s. In contrast, at the same conditions overconsolidated chlorite gouge generally has larger rate-strengthening behavior (a–b = 0.004 to 0.008) between 0.001 and 1 μm/s. At shear displacements greater than 4.9 mm, however, the normally and overconsolidated chlorite gouges sheared at low effective pressure have similar rate-dependencies and dramatically larger rate-strengthening behavior (a–b = 0.010 to 0.028) at velocities less than 1 μm/s (Figure 7b). During individual tests, chlorite layers that are overconsolidated and/or sheared to higher displacements also display different a–b values during steps up and down to the same velocity, which are imposed 1–2.25 mm of slip apart one another. Specifically, increases in shear velocity at greater displacements or strains repeatedly yield higher a–b values than decreases to the same velocity which are imposed at lower displacements (Figures 7a and 7b). However, down-steps in velocity from 10 to 1 μm/s produce large rate-weakening behavior (a–b = −0.015 to −0.006), despite occurring at higher displacements compared to previous rate steps from 0.1 to 1 μm/s that yield rate-strengthening behavior (a–b = 0.005 to 0.008).

In contrast to chlorite gouge, the celadonite gouge rate-strengthens (a–b = 0.004 to 0.008) across all experimental conditions, and the rate-dependence is largely insensitive to consolidation state and displacement (Figure 7c). At slow velocities (0.001–0.1 μm/s), the rate-strengthening behavior of the celadonite gouge is slightly higher at 80 MPa effective pressure (a–b = 0.007 to 0.008) compared to the celadonite gouge sheared at 20 MPa (a–b = 0.004 to 0.005), regardless of consolidation state. However, with increasing velocity from 1 to 10 μm/s, the celadonite gouge rate-strengthens slightly less at 80 MPa (a–b = 0.004 to 0.005) and rate-strengthens slightly more at 20 MPa when overconsolidated (a–b = 0.007 to 0.008).

4.4. Microstructures

At all conditions, deformation of the chlorite gouge layers is localized to shear bands that range from <5 to few 10 s of microns wide (Figure 8). Most shear bands appear perfectly straight in thin section and have R1 (Riedel)

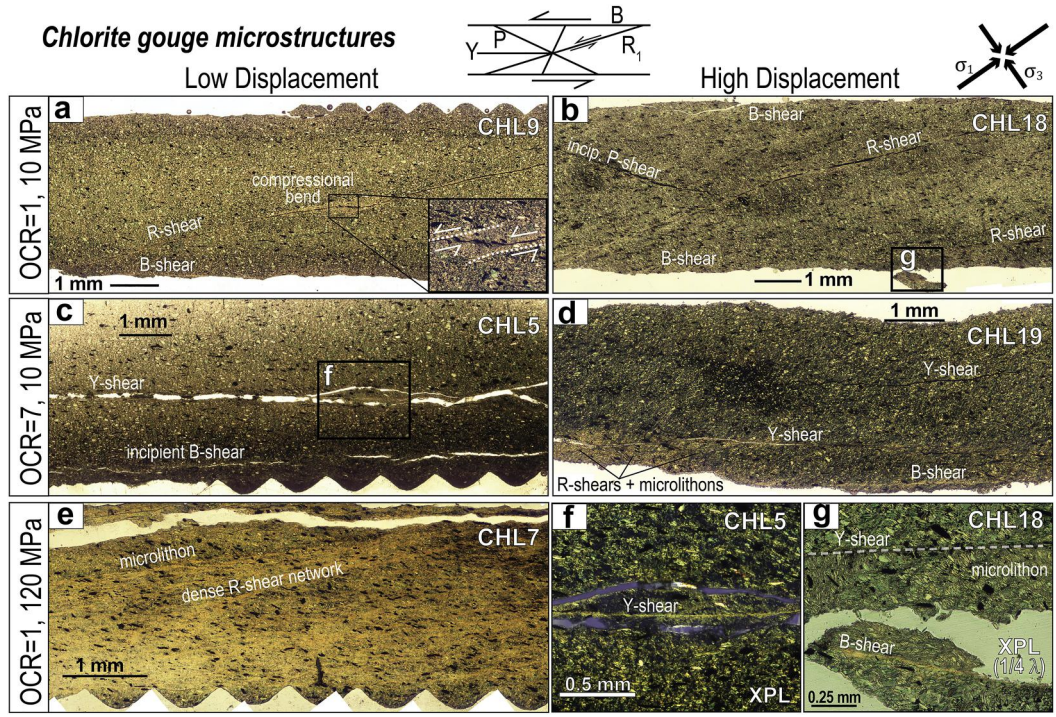

Figure 8. Polarized light photomosaics of chlorite layers after shear deformation with shear band orientations based on the convention of Logan et al. (1979) and Marone and Scholz (1989) and with top to the left shear direction. XPL indicates images taken in cross-polarized light and XPL (1/4 λ) indicates cross-polarized light with the quarter lambda plate inserted. Images without either label were taken in plane polarized light. Normally consolidated chlorite layers sheared at 10 MPa effective pressure are shown in the top panels for (a) low displacement (6.3 mm) and (b) high displacement (10.3 mm), overconsolidated samples (OCR = 7) sheared at 10 MPa for (c) low displacement (6.5 mm) and (d) high displacement (10.3 mm), and normally consolidated chlorite sheared at 120 MPa effective pressure to 7.5 mm shear displacement is shown in (e). (f) Zoomed-in image of the primary Y-shear that developed under overconsolidated and lower displacement conditions (region shown in c). (g) Zoomed-in image of boundary shear and adjacent fabric elements in normally consolidated chlorite sheared to higher displacements.

and Y-orientations (Logan, 1979) (Figures 8a–8d). Shear bands with Y-orientations are primarily boundary shears; however, Y-shears closer to the center of the layers developed in overconsolidated chlorite layers (Figures 8c and 8d). Normally consolidated chlorite gouges primarily develop R1 shear bands which connect into boundary shears.

Chlorite gouge sheared at the lowest effective pressure (10 MPa) developed the fewest shears independent of consolidation state and the abundance of shears increases slightly with displacement. The overconsolidated sample sheared to lower displacements (6.5 mm) concentrates deformation along a Y-shear band near the center of the gouge layer (Figures 8c and 8f), whereas at higher displacements (10.3 mm), boundary shears become more pronounced and cause subsidiary networks of R1 and/or Y-shears to develop adjacent to them (Figure 8d). Although normally consolidated chlorite gouge also develops more mature boundary shears at higher displacements (10.3 mm), Y-shear bands are absent (Figures 8a and 8b). The abundance of shear bands increases dramatically with increasing effective pressure, which is evident in the high density of Riedel shears that developed at 120 MPa effective pressure (Figure 8e). Riedel and boundary-parallel shear bands display more uniform birefringence in polarized light and have an overall sharper appearance in gouges that were overconsolidated and/or sheared at high effective pressure or displacements (Figures 8e-8g). At these conditions, microlithons develop in regions between adjacent and parallel shear bands, in which ilmenite grains and densely packed chlorite plates rotate toward the P-orientation (Figures 8e and 8g).

Like the chlorite samples, the celadonite gouge also develops networks of Y- and R1 shears; however, the structures that develop in celadonite gouge are insensitive to consolidation path and have different physical characteristics (Figure 9). Both overconsolidated and normally consolidated celadonite gouges form several

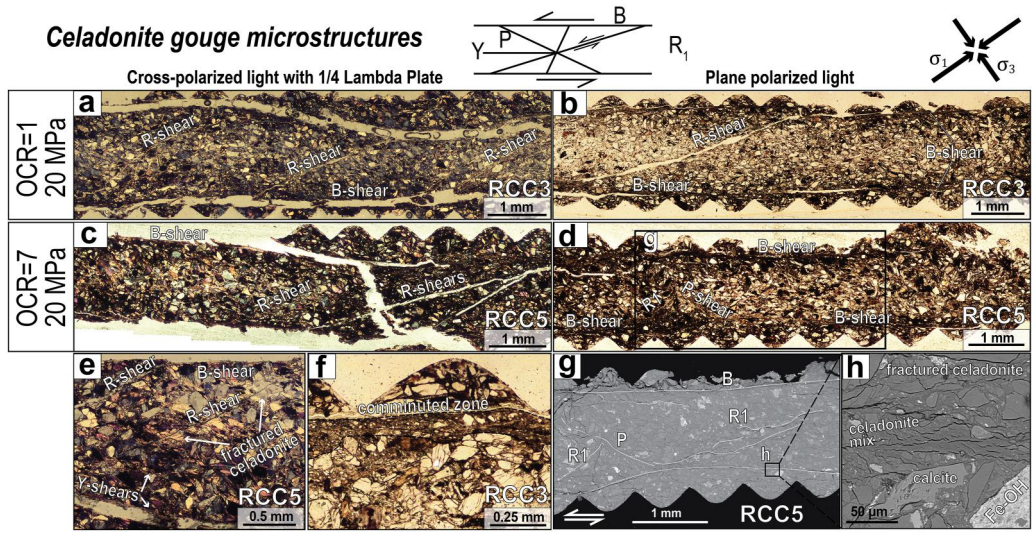

Figure 9. Polarized light photomosaics of celadonite layers with shear direction top to the left. Top row: normally consolidated sample (OCR = 1) sheared at 20 MPa effective pressure under (a) cross-polarized light with the ¼ lambda plate inserted and (b) plane polarized light. Middle row: overconsolidated celadonite sample (OCR = 7) under (c) cross-polarized light with the ¼ lambda plate inserted and (d) plane polarized light. Bottom row: (e) magnified image of overconsolidated celadonite sample from separate area in sample showing relationships between shear bands and clasts, (f) magnified image of cataclastic boundary shear band in normally consolidated sample (RCC3), (g) back-scattered SEM image of region in sample RCC5, and (h) zoomed-in image of boundary-parallel shear band.

Riedel shear bands which propagate through the layer as well as subsidiary shear bands or splays (Figures 9a–9d). The celadonite gouges contain both straight and curved R1 shear bands, tens of microns wide, which split and wrap around large clasts (Figures 9a and 9c) or fracture through them (Figure 9e). In addition, both overconsolidated and normally consolidated samples form straight to gently anastomosing boundary shear bands which continue along most of the entire length of the saw-cut boundaries and vary between 10 s to several 100 s of microns in width (Figures 9a–9f). These boundary-parallel shear bands in the celadonite gouge occur as zones of localized comminution (Figure 9f), containing narrower zones within them where subparallel shear surfaces fracture clasts of celadonite and coalesce in extremely fine-grained celadonite mixtures (Figures 9g and 9h). We were unable to preserve the sample sheared at higher effective pressure (RCC6) for comparison.

5. Discussion

5.1. Stress Path Effects on Mechanical Behavior

The strengths of the overconsolidated and normally consolidated samples are generally consistent with sediment mechanics predictions for these endmember stress paths during an evolution toward critical state (Figures 1b and 5). However, stress path effects on the strength of the celadonite gouges are limited to lower shear displacements than we observe for the simulated chlorite gouges (Figures 4b and 4c). This correlates with pore volume changes and microstructural changes that are less sensitive to consolidation state in the celadonite gouge compared to chlorite layers.

Chlorite gouges normally consolidated at all effective pressures, and therefore pore pressures, exhibit nonlinear to linear strain-hardening trends, consistent with normal consolidation and shear in the ductile regime (Figures 1b and 4). We propose that although chlorite layers reach critical state at the lowest effective stress (highest pore fluid pressure), at the highest effective pressures (lowest pore fluid pressures) (i.e., σ_3' = 70 and 120 MPa) the chlorite gouge continuously strain-hardens throughout the experiments without reaching critical state due to differences in the evolution of porosity and/or fabric (Figure 5).

Our measurements of pore volume reduction during shear at 120 MPa effective pressure (Figures 6b and 6c) and microscale observations of pervasive grain size reduction and abundant Riedel shears (Figure 8e) suggest that strain-hardening in the chlorite layers results from persistent grain crushing and pore collapse as previously

interpreted in chlorite gouges deformed at similar effective stresses (Haines et al., 2013) and/or the continuous development of new Riedel shears. Although strain-hardening may also be promoted by the relatively thick layers of chlorite (~3 mm at the start of triaxial loading), which could require higher shear displacements than we achieved to reach critical state shearing, previous work indicates strain-hardening can persist to much higher strains. For example, unsaturated chlorite layers with similar thickness and particle size distribution as our samples developed similar deformation textures while continually strain-hardening to shear strains approaching 20 at effective normal stresses greater than 20 MPa, but not at lower stresses at which steady-state frictional sliding occurred at much lower strains (Haines et al., 2013).

By comparison, at low effective stress (10 MPa), the broad transition from strain-hardening to weakening and then steady-state shearing in normally consolidated chlorite layers corresponds to significantly less grain size reduction and fewer Riedel shears than formed at higher effective pressures (Figures 8a and 8b). This supports the interpretation that persistent cataclasis and shear development are strain-hardening processes that are required to reach steady-state at high effective pressure. The fact that the number and orientations of Riedel shears are similar in samples sheared to 6.3 and 10.3 mm at 10 MPa effective pressure suggests that, at steady-state, slip continues preferentially along the same shears, which also supports this interpretation. Although the displacement required to reach steady-state is different for the two normally consolidated layers sheared at 10 MPa effective pressure (CHL9 and CHL18), their peak (0.57) and steady-state (0.52) frictional strengths are very similar as is the displacement over which they weaken (Figures 4b and 4d). This consistency in the strain-weakening behavior of normally consolidated and overpressured chlorite layers likely indicates gradual strain-localization, which is associated with strain-weakening (e.g., Haines et al., 2013; Hall et al., 2012; Niemeijer et al., 2010), despite being normally compacted prior to triaxial loading. For instance, Haines et al. (2013) illustrated that strain-weakening in phyllosilicate-rich fault gouges occurs during the propagation of Riedel shears across the layer and growth of boundary shears. From our microstructural observations, we similarly find throughgoing Riedel shears and boundary shears that developed in normally consolidated chlorite gouge sheared at 10 MPa effective pressure (Figures 8a and 8b). As such, the nucleation and propagation of these shears may have facilitated their gradual strain-weakening behavior prior to reaching steady-state sliding (Figures 4b and 4d). Alternatively, we note that strain-weakening may occur in low permeability gouges if pore fluids are undrained and compaction results in fluid overpressure (e.g., Faulkner et al., 2018; Fischer & Paterson, 1989). However, this is unlikely responsible for strain-weakening in our experiments because our conservative estimates show they are drained below shearing rates of 8.1 μm/s and strain-weakening occurs at both steps up and down in shearing rate.

The evolution in the strength of overconsolidated chlorite layers with strain is consistent with deformation in the brittle field of the critical state sediment mechanics envelope. Although the two stages of strain-weakening that we document are not predicted by CSSM, the correlations between strength evolution and volume strain are consistent. In particular, our observations of enhanced dilation during deformation to peak strength and during subsequent strain-weakening, followed by nearly constant pore volume with slip during the first phase of steady-state sliding are predicted by CSSM and occur during localization (Figure 6d). However, the resumed dilation that we observe during the second stage of strain-weakening indicates a two-stage localization process in the over-consolidated chlorite layers. We speculate that these two stages of strain-weakening may be reflected by microstructural differences between samples CHL5 and CHL19, which were both overconsolidated yet sheared to 6.5 and 10.3 mm, respectively. With increasing displacement, strain localization primarily shifts from one Y-shear within the middle of CHL5 (Figure 8c) to boundary shears that become more pronounced in CHL19 (Figure 8d). If we assume that strain-weakening correlates with strain localization onto newly forming shear bands, we can envision that the first stage of strain-weakening from the initial peak strength may have occurred during Y-shear nucleation and propagation. After propagating through the gouge layer, the Y-shear could have then accommodated steady-state sliding behavior in the samples until ~1.4 mm of displacement. Subsequently, boundary shears propagated along the edges of the sample, which contributed to the second stage of strain-weakening.

In comparison to the chlorite layers, the mechanical behavior of the celadonite is significantly less sensitive to consolidation state (Figure 4). Although the overconsolidated celadonite shows an initial peak in strength and a strain-weakening phase consistent with the chlorite and CSSM in the brittle field, its subsequent strain-hardening is very similar to the behavior of normally consolidated celadonite and CSSM in the ductile field (Figure 4). Furthermore, the evolution from strain-hardening to strain-weakening at the lowest effective pressures is similar to the second strain-weakening event in the chlorite, but unlike chlorite it occurs for both consolidation states.

Consistent with CSSM and the chlorite layers, the transition to strain-weakening correlates with a transition to dilation in both overconsolidated and normally consolidated celadonite, indicating strain localization (Figure 6d).

The relative insensitivity of the celadonite strength to consolidation state at displacements greater than 1 mm is reflected in the relative independence of the microstructural evolution on consolidation state and stress path (Figure 9). In particular, deformation in both normally and overconsolidated celadonite predominantly occurs within cataclastic boundary shear bands that propagate along the full length of the layers and along major or subsidiary Riedel shears that fracture and wrap around clasts. Because shears concentrate in finer-grained material and typically curve around larger clasts, we hypothesize that the similar abundance, geometry, and texture of microstructures that develop in both samples result from the greater abundance of larger clasts in the sample (e.g., Figures 2b and 9), which exert greater control on shear propagation and development than past stress state. In contrast, we hypothesize that localization in the chlorite layers, which contain less coarse-sized grains and is more homogeneous, is controlled primarily by the consolidation state. As a result, we infer that the development of localized shears controls the strength, both of which are less sensitive to path in the celadonite compared to the chlorite layers.

We interpret that strain-hardening and concomitant compaction in the celadonite gouge are caused by pore collapse and cataclasis which occur during distributed ductile deformation. In contrast, strain-weakening and dilatancy are linked to localization of deformation along shears consistent with CSSM. We postulate that the observed strain-weakening and dilation in the celadonite gouge at low effective pressure may have occurred through the propagation of upper and lower boundary shears along the length of the celadonite layer, as indicated in the chlorite layers. However, we did not conduct additional experiments on the celadonite at lower displacements to verify this and were unable to preserve the sample sheared at higher effective pressure, which did not strain-weaken or dilate, for comparison.

5.2. Path-Dependent Rate-Dependence

Like the evolution of strength with displacement, the dependence of strength on deformation rate is much more influenced by path in the chlorite gouge layers than in the celadonite gouge. Specifically, whereas the rate-dependence of the celadonite strength does not depend on path (Figure 7c), the rate-dependence of chlorite strength is path dependent at displacements less than 5 mm consistent with the much more path-dependent strength for chlorite at displacements less than 5 mm (Figures 7a and 7b). In the celadonite gouge, we attribute the path independence of the rate-dependence to the similar microstructural evolution at different consolidation states. For chlorite, whose microstructural evolution does depend on consolidation state we evaluate different ways that the microstructures may influence the rate-dependence.

One possible explanation for why the rate dependencies evolve toward similar values in overconsolidated and normally consolidated layers of chlorite sheared at high pore fluid pressure (Figure 7b) is that they achieve the same porosity once enough strain is accommodated to reach critical state. Porosity has been shown to play a key role in determining the slip behavior of granular gouges (e.g., Marone et al., 1990). However, we infer that porosity evolution by itself is unlikely to cause the converging frictional behavior of the chlorite layers, because significant dilation of the overconsolidated sample would be required for its porosity to become equal to that of the normally consolidated sample during shear. Specifically, the pore volume of the overconsolidated samples decrease 1 cm^3 during consolidation from 10 to 70 MPa effective pressure, indicating that it initially has 1 cm^3 less pore volume than the normally consolidated sample (Figure 6a). However, during subsequent triaxial loading and shear deformation, the pore fluid volume in the normally consolidated sample only decreases by ~0.6 cm^3, while the overconsolidated sample displays relatively minimal volume change (Figure 6b). This implies that the normally consolidated chlorite layers still have greater porosity (or ~0.4 cm^3 greater pore volume) than the overconsolidated chlorite at the end of the experiments. Lastly, at high displacements and 10 MPa effective pressure, normally consolidated chlorite (CHL18) exhibits greater rate-strengthening behavior at slow slip rates (<1 μm/s) than overconsolidated chlorite sheared at lower displacements (CHL5) (7a and 7b). This indicates that porosity reduction cannot solely account for the increased rate-strengthening behavior of sample CHL18.

Alternatively, the development of similar deformation textures with increasing strain, such as the number, orientation, and spatial distribution of shear bands, may control their coinciding slip behaviors (e.g., Moore et al., 1989), irrespective of whether their total porosities become equal. We interpret that the similar rate-dependence and strength of normally consolidated and overconsolidated chlorite at the greatest displacements

are most likely controlled by their similar styles of shear localization. Whereas a dense network of shear bands develops at higher pressures, shear localizes onto relatively few R and Y shears at low effective pressure, regardless of consolidation state. However, when the sample is overconsolidated, less displacement or shear strain is required to produce these structures (e.g., samples CHL5 and CHL9 in Figure 8). Our observation that fewer shears correlates with greater rate-strengthening behavior of chlorite may indicate that continual slip along one or a few shear surfaces could prevent significant evolution in contact area or strength between aligned platy chlorite surfaces. In contrast, deformation that is distributed along many shear surfaces that individually accommodate less displacement and may become dis- or reactivated during bulk shearing of the gouge, increases the evolutionary effect promoting rate-weakening behavior.

In an earlier study, we proposed that time-dependent removal of adsorbed water between aligned chlorite surfaces could lead to rate-weakening behavior (Belzer & French, 2022). Here, we show that a significant increase in a-b in chlorite from low to high displacements at 10 MPa effective pressure (Figures 7a and 7b) correlates with a decrease in slip-dependent compaction (Figures 6b and 6c), accompanied by a gradual transition from strain-hardening behavior to steady-state frictional sliding (Figures 4b and 4d). These observations are consistent with the water film hypothesis (Scruggs, 1997) whereby at low strains water layers may progressively squeeze out as the sample compacts, leading to a greater evolution effect and rate-weakening behavior, whereas at higher strains water layer thickness remains relatively constant with slip, limiting the evolution effect and promoting rate-strengthening behavior. Alternatively, compaction may promote time-dependent hardening of aligned mineral surfaces independent of losing adsorbed water. Compaction and strain-hardening behavior in muscovite and chlorite-rich gouges have also been associated with pervasive and localized cataclasis leading to a dense network of anastomosing shear bands (e.g., Haines et al., 2013; Van Diggelen et al., 2010), consistent with the microstructures and mechanical behavior that we observe in chlorite at 70 and 120 MPa effective pressure. Independent of contact-scale effects of adsorbed water (e.g., Israelachvili et al., 1988; Moore & Lockner, 2004), the occurrence of cataclastic processes in the chlorite layer during compaction and strain-hardening may also impact its rate-weakening behavior. Notably, at >20 MPa effective pressure, this style of fabric and strength evolution continues in sheared layers of chlorite to much higher shear strains of ∼20 (Haines et al., 2013). This suggests that at high effective pressure, chlorite could sustain rate-weakening behavior to significantly greater amounts of slip than it is able to sustain at low effective pressure (or excess pore fluid pressure). However, we note that the influence of cataclasis, compaction, and strain-hardening on the rate-dependence of phyllosilicate-rich gouges depends on their mineralogy and/or particle size distribution, as contrastingly, the celadonites sheared in our study rate-strengthen in tandem with similar microstructural processes and deformation responses.

5.3. Implications for the Shallow Megathrust

The mechanics that control mode of slip along the shallow megathrust are debated. However, several of the existing hypotheses call upon the roles of elevated fluid pressure, as inferred from geophysical and geological observations (e.g., Bangs et al., 2023; Bassett et al., 2014; Chesley et al., 2021; Ellis et al., 2015; Husker et al., 2017; Kitajima & Saffer, 2012; Kodaira et al., 2004; Li et al., 2018; Liu & Rice, 2005, 2007; Rubin, 2008; Saffer & Wallace, 2015). Our results indicate that the role of elevated fluid pressure on the mechanics of fault slip depends on the process that generates overpressure and the resulting effective stress path. In addition, the composition and microstructure of the fault rock hosting slip also imparts a control on the importance of effective stress path on controlling slip. Although total slip during our experiments is relatively small, it is a non-negligible component of several slow modes of fault slip including slow slip and low-frequency earthquakes (e.g., Fagereng et al., 2011; Thomas et al., 2016; Ujiie et al., 2018). Thus, the path dependent mechanical and frictional behavior that we observe at displacements less than 1–5 mm may impart a control on transient fault deformation.

The frictional rate-dependence of faults is commonly proposed to control their mode of slip (e.g., Liu & Rice, 2005, 2007; Rubin, 2008; Scholz, 1998; Shibazaki & Iio, 2003; Shibazaki & Shimamoto, 2007; Skarbek et al., 2012). Our study indicates that normally consolidated chlorite-rich fault rock, when sheared at high pore fluid pressures associated with disequilibrium compaction or at low pore pressures reflecting consolidated and dewatered material along the plate boundary, can promote rate-neutral or slightly rate-weakening behavior of faults at slow slip speeds (e.g., $\sim 10^{-8}$ to 10^{-7} m/s) (Figure 7a), which is one condition proposed to facilitate episodic slow slip (Rubin, 2008). In contrast, overconsolidated chlorite-rich fault rock promotes larger rate-strengthening behavior at those slip speeds, suggesting that elevated fluid pressures sourced from dehydration

reactions promote stable slip at those velocities more effectively due to retained memory of stress in fault rock microstructure.

However, we observe that at high pore fluid pressure, rate-strengthening in both overconsolidated and normally consolidated chlorite-rich fault gouge also increases dramatically with increasing shear displacement, such that after ~5 mm of displacement its frictional rate-dependence is no longer influenced by consolidation history (Figure 7b). Several models of slow slip and tremor using the rate-and-state framework have incorporated possible stabilizing mechanisms of fault slip, such as using materials that rate-weaken at low velocities of fault slip and transition to rate-strengthening behavior with increasing velocity (Hawthorne & Rubin, 2013; Shibazaki & Iio, 2003; Shibazaki & Shimamoto, 2007)—which we observe in sheared chlorite layers at 70 and 120 MPa effective pressure—or allowing dilatant hardening during slip (Liu, 2013; Segall et al., 2010). Likewise, our results suggest that in overpressured phyllosilicate-dominated fault zones, rate-weakening at low displacements could give rise to significant rate-strengthening behavior at higher displacements to stabilize slip.

In addition, path-dependent deformation could significantly influence the apparent frictional behavior of natural shear zones under undrained pore fluid pressure conditions. Based on CSSM predictions, undrained materials that are normally consolidated are likely to compact during deformation, which can increase fluid pressure further weakening shear zones. In contrast, undrained and overconsolidated fine-grained materials are likely to exhibit shear-induced dilation while evolving to steady-state, favoring dilatant hardening which is proposed to result in slow earthquakes (Liu, 2013; Segall et al., 2010). As highlighted in previous work, inefficient draining of pore pressure can give rise to anomalous frictional behavior in fine-grained and low-permeability fault gouges (e.g., Faulkner et al., 2018; Morrow et al., 2017); for example, intrinsically rate-strengthening materials have been shown to display apparent rate-weakening behavior during compaction-driven fluid overpressure (Faulkner et al., 2018). We observe significant rate-weakening behavior in chlorite ($a–b = -0.006$ to -0.015) at 10 MPa effective pressure (120 MPa pore pressure) during all down steps in shear velocity from 10 to 1 μm/s. This could reflect a shift from potentially undrained to drained conditions, as the initial velocity is higher than the maximum fluid diffusion rate (8.1 μm/s) that we calculated earlier for the sample. In other words, the negative rate-dependence could occur if excess pore pressure in the gouge dissipates following the decrease in velocity, leading to an apparent increase in strength. In addition, the largest rate-weakening behavior (-0.015) is observed in the normally consolidated sample at lower displacements (5.1 mm), while its compaction rate is higher than that of the other samples, and as it strain-weakens. These observations indicate that the chlorite gouge is inefficiently drained during rate steps from 10 to 1 μm/s and that its apparent slip behavior is also path and strain dependent. Our experimental results therefore provide insights into how stress path effects on rate-dependence can modify the behavior of faults under both drained and undrained pore pressure conditions.

Exhumed subduction thrust zones that deformed under the source conditions of active shallow slow earthquakes often record localized slip along multiple high-strain and discrete structures such as foliated phyllosilicate-rich shear bands and/or cataclastic bands (Kirkpatrick et al., 2021). These fault rocks are commonly enriched in phyllosilicates, including chlorite when derived from subducting basalt (e.g., Leah et al., 2022; Phillips et al., 2020), and accommodate slip through brittle or semi-brittle deformation mechanisms. From our study, the path-dependent frictional behavior of simulated chlorite gouge suggests that natural chlorite-rich shear bands could accommodate slow and transient modes of slip, whereas the path-independent behavior of the celadonite gouge suggests that shear bands dominated by other phyllosilicate minerals (e.g., celadonite) and/or cataclastic bands may not. Our microstructural observations indicate that deformation of the chlorite gouge is primarily accommodated by contact-scale frictional deformation mechanisms within narrow bands of well aligned chlorite sheets, whereas the clast-bearing celadonite gouge develops wider shear bands which accommodate deformation through cataclastic flow. These contrasting mechanisms of shear localization might control their different path- or slip-dependencies of frictional behavior, which would have implications for assessing the potential of natural fault rock to host transient and slow modes of slip. However, further experimental studies are required to differentiate and fully understand the effects of composition, grain size distribution, and microstructure on path- or slip-dependent frictional deformation of fault rock.

6. Conclusions

Recent work has presented conflicting evidence for whether elevated pore fluid pressure tends to stabilize or destabilize fault slip. Furthermore, elevated pore fluid pressure is proposed to control the speed and mode of slip

along the shallow megathrust. However, the processes that contribute to pore fluid overpressure in the shallow subduction zone, disequilibrium compaction and dehydration reactions, lead to significantly different effective stress paths. We present an experimental study of the role of effective stress path leading to pore fluid pressurization on the mechanical properties of fault rocks representative of the shallow subduction megathrust. Our experiments on two simulated fault gouges, a chlorite-rich gouge representing a phyllosilicate-dominated fault rock and a celadonite-rich cataclasite from the Rodeo cove thrust representing a clast-bearing fault rock, show that the effects of pore fluid pressure is dependent on both the effective stress path taken toward overpressurization and the microstructure of the fault rock. We find that, to a first order, critical state soil mechanics (CSSM) provides a useful framework for predicting the role of effective stress path on the strength evolution and volumetric strain of both fault rocks. However, we find that the effects of path are more pronounced and persist to greater displacements in phyllosilicate-dominated fault rocks whose microstructure is more influenced by consolidation state and stress path. In addition, the effects of path on microstructure and strength, also impart a much more significant control on the rate-dependence of strength in phyllosilicate-dominated fault rocks than in clast-bearing fault rocks, which is not predicted by CSSM.

Our study indicates that chlorite-rich fault rocks which experience high pore fluid pressure through disequilibrium compaction have rate-neutral or slightly rate-weakening behavior at low slip speeds relevant to slow earthquakes, particularly at low shear displacements (<5 mm). This could promote unstable slip at the shallowest extent of subduction megathrusts. In contrast, overconsolidation linked to dehydration-induced fluid overpressure tends to promote larger rate-strengthening behavior at the same conditions, due to preserved memory of stress in its microstructure, favoring more stable modes of slip further downdip along the plate boundary. Independent of effective stress path, elevated pore fluid pressure could also cause a significant increase in the rate-strengthening behavior of phyllosilicate-dominated fault rock with increasing slip, which may serve to stabilize transient slip modes in overpressured shear zones.

Data Availability Statement

The experimental data used in this paper are available at Belzer and French (2024).

Acknowledgments
This work was funded by NSF EAR-1945264 to MF and a GSA Student Research Grant to BB. We thank the Shared Equipment Authority at Rice University, Houston, TX for use of the SEM and Will Larsen and Debadrita Jana for their help performing laser particle size analysis.

References

Abdulkarim, M., Grema, H. M., Adamu, I. H., Mueller, D., Schulz, M., Ulbrich, M., et al. (2021). Effect of using different chemical dispersing agents in grain size analyses of fluvial sediments via laser diffraction spectrometry. *Methods and Protocols*, *4*(3), 44. https://doi.org/10.3390/mps4030044

Bangs, N. L., Morgan, J. K., Bell, R. E., Han, S., Arai, R., Kodaira, S., et al. (2023). Slow slip along the Hikurangi margin linked to fluid-rich sediments trailing subducting seamounts. *Nature Geoscience*, *16*(6), 505–512. https://doi.org/10.1038/s41561-023-01186-3

Bassett, D., Sutherland, R., & Henrys, S. (2014). Slow wavespeeds and fluid overpressure in a region of shallow geodetic locking and slow slip, Hikurangi subduction margin, New Zealand. *Earth and Planetary Science Letters*, *389*, 1–13. https://doi.org/10.1016/j.epsl.2013.12.021

Bedford, J. D., Faulkner, D. R., Allen, M. J., & Hirose, T. (2021). The stabilizing effect of high pore-fluid pressure along subduction megathrust faults: Evidence from friction experiments on accretionary sediments from the Nankai Trough. *Earth and Planetary Science Letters*, *574*, 117161. https://doi.org/10.1016/j.epsl.2021.117161

Beeler, N. M., Thomas, A., Bürgmann, R., & Shelly, D. (2013). Inferring fault rheology from low-frequency earthquakes on the San Andreas. *Journal of Geophysical Research: Solid Earth*, *118*(11), 5976–5990. https://doi.org/10.1002/2013jb010118

Belzer, B., & French, M. (2024). Path and slip dependent behavior of shallow subduction shear zones during fluid overpressure (Version v2) [Dataset]. *Zenodo*. https://doi.org/10.5281/zenodo.8156673

Belzer, B. D., & French, M. E. (2022). Frictional constitutive behavior of chlorite at low shearing rates and hydrothermal conditions. *Tectonophysics*, *837*, 229435. https://doi.org/10.1016/j.tecto.2022.229435

Bilek, S. L., & Lay, T. (1999). Rigidity variations with depth along interplate megathrust faults in subduction zones. *Nature*, *400*(6743), 443–446. https://doi.org/10.1038/22739

Byerlee, J. (1990). Friction, overpressure and fault normal compression. *Geophysical Research Letters*, *17*(12), 2109–2112. https://doi.org/10.1029/gl017i012p02109

Chesley, C., Naif, S., Key, K., & Bassett, D. (2021). Fluid-rich subducting topography generates anomalous forearc porosity. *Nature*, *595*(7866), 255–260. https://doi.org/10.1038/s41586-021-03619-8

Chester, F. M. (1994). Effects of temperature on friction: Constitutive equations and experiments with quartz gouge. *Journal of Geophysical Research*, *99*(B4), 7247–7261. https://doi.org/10.1029/93jb03110

den Hartog, S. A., & Spiers, C. J. (2013). Influence of subduction zone conditions and gouge composition on frictional slip stability of megathrust faults. *Tectonophysics*, *600*, 75–90. https://doi.org/10.1016/j.tecto.2012.11.006

Dieterich, J. H. (1978). Time-dependent friction and the mechanics of stick-slip. *Rock Friction and Earthquake Prediction*, 790–806. https://doi.org/10.1007/978-3-0348-7182-2_15

Dieterich, J. H. (1979). Modeling of rock friction: 1. Experimental results and constitutive equations. *Journal of Geophysical Research*, *84*(B5), 2161–2168. https://doi.org/10.1029/jb084ib05p02161

Ellis, S., Fagereng, Å., Barker, D., Henrys, S., Saffer, D., Wallace, L., et al. (2015). Fluid budgets along the northern Hikurangi subduction margin, New Zealand: The effect of a subducting seamount on fluid pressure. *Geophysical Journal International*, *202*(1), 277–297. https://doi.org/10.1093/gji/ggv127

Ellsworth, W. L. (2013). Injection-induced earthquakes. *Science*, *341*(6142), 1225942. https://doi.org/10.1126/science.1225942

Fagereng, Å., Remitti, F., & Sibson, R. H. (2011). Incrementally developed slickenfibers—Geological record of repeating low stress-drop seismic events? *Tectonophysics*, *510*(3), 381–386. https://doi.org/10.1016/j.tecto.2011.08.015

Faulkner, D. R., & Rutter, E. H. (2003). The effect of temperature, the nature of the pore fluid, and subyield differential stress on the permeability of phyllosilicate-rich fault gouge. *Journal of Geophysical Research*, *108*(B5). https://doi.org/10.1029/2001jb001581

Faulkner, D. R., Sanchez-Roa, C., Boulton, C., & Den Hartog, S. A. M. (2018). Pore fluid pressure development in compacting fault gouge in theory, experiments, and nature. *Journal of Geophysical Research: Solid Earth*, *123*(1), 226–241. https://doi.org/10.1002/2017jb015130

Fischer, G. J., & Paterson, M. S. (1989). Dilatancy during rock deformation at high temperatures and pressures. *Journal of Geophysical Research*, *94*(B12), 17607–17617. https://doi.org/10.1029/JB094iB12p17607

Hacker, B. R., Peacock, S. M., Abers, G. A., & Holloway, S. D. (2003). Subduction factory 2. Are intermediate-depth earthquakes in subducting slabs linked to metamorphic dehydration reactions? *Journal of Geophysical Research*, *108*(B1). https://doi.org/10.1029/2001jb001129

Haines, S. H., Kaproth, B., Marone, C., Saffer, D., & van der Pluijm, B. (2013). Shear zones in clay-rich fault gouge: A laboratory study of fabric development and evolution. *Journal of Structural Geology*, *51*, 206–225. https://doi.org/10.1016/j.jsg.2013.01.002

Hall, S. A., Desrues, J., Viggiani, G., Bésuelle, P., & Andò, E. (2012). Experimental characterisation of (localised) deformation phenomena in granular geomaterials from sample down to inter-and intra-grain scales. *Procedia IUTAM*, *4*, 54–65. https://doi.org/10.1016/j.piutam.2012.05.007

Hawthorne, J. C., & Rubin, A. M. (2013). Laterally propagating slow slip events in a rate and state friction model with a velocity-weakening to velocity-strengthening transition. *Journal of Geophysical Research: Solid Earth*, *118*(7), 3785–3808. https://doi.org/10.1002/jgrb.50261

Husker, A., Ferrari, L., Arango-Galván, C., Corbo-Camargo, F., & Arzate-Flores, J. A. (2017). A geologic recipe for transient slip within the seismogenic zone: Insight from the Guerrero seismic gap, Mexico. *Geology*, *46*(1), 35–38. https://doi.org/10.1130/G39202.1

Ikari, M. J., Saffer, D. M., & Marone, C. (2009). Frictional and hydrologic properties of clay-rich fault gouge. *Journal of Geophysical Research*, *114*(B5). https://doi.org/10.1029/2008jb006089

Israelachvili, J. N., McGuiggan, P. M., & Homola, A. M. (1988). Dynamic properties of molecularly thin liquid films. *Science*, *240*(4849), 189–191. https://doi.org/10.1126/science.240.4849.189

Jones, M. (1994). Mechanical principles of sediment deformation. In *The geological deformation of sediments* (pp. 37–71). Springer.

Karig, D., & Morgan, J. (1994). Tectonic deformation: Stress paths and strain histories. In *The geological deformation of sediments* (pp. 167–204). Springer.

Karner, S. L., Chester, F. M., & Chester, J. S. (2005). Towards a general state-variable constitutive relation to describe granular deformation. *Earth and Planetary Science Letters*, *237*(3–4), 940–950. https://doi.org/10.1016/j.epsl.2005.06.056

King Hubbert, M., & Rubey, W. W. (1959). Role of fluid pressure in mechanics of overthrust faulting: I. Mechanics of fluid-filled porous solids and its application to overthrust faulting. *Geological Society of America Bulletin*, *70*(2), 115–166. https://doi.org/10.1130/0016-7606(1959)70[115:rofpim]2.0.co;2

Kirkpatrick, J. D., Fagereng, Å., & Shelly, D. R. (2021). Geological constraints on the mechanisms of slow earthquakes. *Nature Reviews Earth and Environment*, *2*(4), 285–301. https://doi.org/10.1038/s43017-021-00148-w

Kitajima, H., Chester, F. M., & Biscontin, G. (2012). Mechanical and hydraulic properties of Nankai accretionary prism sediments: Effect of stress path. *Geochemistry, Geophysics, Geosystems*, *13*(10). https://doi.org/10.1029/2012gc004124

Kitajima, H., & Saffer, D. M. (2012). Elevated pore pressure and anomalously low stress in regions of low frequency earthquakes along the Nankai Trough subduction megathrust. *Geophysical Research Letters*, *39*(23). https://doi.org/10.1029/2012GL053793

Kodaira, S., Iidaka, T., Kato, A., Park, J.-O., Iwasaki, T., & Kaneda, Y. (2004). High pore fluid pressure may cause silent slip in the Nankai Trough. *Science*, *304*(5675), 1295–1298. https://doi.org/10.1126/science.1096535

Leah, H., Fagereng, Å., Groome, N., Buchs, D., Eijsink, A., & Niemeijer, A. (2022). Heterogeneous subgreenschist deformation in an exhumed sediment-poor mélange. *Journal of Geophysical Research: Solid Earth*, *127*(8), e2022JB024353. https://doi.org/10.1029/2022JB024353

Li, J., Shillington, D. J., Saffer, D. M., Bécel, A., Nedimović, M. R., Kuehn, H., et al. (2018). Connections between subducted sediment, pore-fluid pressure, and earthquake behavior along the Alaska megathrust. *Geology*, *46*(4), 299–302. https://doi.org/10.1130/G39557.1

Liu, Y. (2013). Numerical simulations on megathrust rupture stabilized under strong dilatancy strengthening in slow slip region. *Geophysical Research Letters*, *40*(7), 1311–1316. https://doi.org/10.1002/grl.50298

Liu, Y., & Rice, J. R. (2005). Aseismic slip transients emerge spontaneously in three-dimensional rate and state modeling of subduction earthquake sequences. *Journal of Geophysical Research*, *110*(B8). https://doi.org/10.1029/2004JB003424

Liu, Y., & Rice, J. R. (2007). Spontaneous and triggered aseismic deformation transients in a subduction fault model. *Journal of Geophysical Research*, *112*(B9). https://doi.org/10.1029/2007JB004930

Logan, J. M. (1979). Experimental studies of simulated gouge and their application to studies of natural fault gouge. *Analysis of Actual Fault Zones in Bedrock*, 305–343.

Logan, J. M., Friedman, M., Higgs, N., Dengo, C., & Shimamoto, T. (1979). Experimental studies of simulated gouge and their application to studies of natural fault zones Open File Rep. In *Proceedings of Conference VIII: Analysis of actual fault zones in bedrock* (Vol. 79–1239, pp. 305–343). U.S. Geological Survey.

Marone, C., Raleigh, C. B., & Scholz, C. H. (1990). Frictional behavior and constitutive modeling of simulated fault gouge. *Journal of Geophysical Research*, *95*(B5), 7007–7025. https://doi.org/10.1029/jb095ib05p07007

Marone, C., & Scholz, C. H. (1989). Particle-size distribution and microstructures within simulated fault gouge. *Journal of Structural Geology*, *11*(7), 799–814. https://doi.org/10.1016/0191-8141(89)90099-0

Meneghini, F., & Moore, J. C. (2007). Deformation and hydrofracture in a subduction thrust at seismogenic depths: The Rodeo Cove thrust zone, Marin Headlands, California. *Geological Society of America Bulletin*, *119*(1–2), 174–183. https://doi.org/10.1130/b25807.1

Moore, D. E., & Lockner, D. A. (2004). Crystallographic controls on the frictional behavior of dry and water-saturated sheet structure minerals. *Journal of Geophysical Research*, *109*(B3). https://doi.org/10.1029/2003JB002582

Moore, D. E., Summers, R., & Byerlee, J. D. (1989). Sliding behavior and deformation textures of heated illite gouge. *Journal of Structural Geology*, *11*(3), 329–342. https://doi.org/10.1016/0191-8141(89)90072-2

Morrow, C. A., Moore, D. E., & Lockner, D. A. (2017). Frictional strength of wet and dry montmorillonite. *Journal of Geophysical Research: Solid Earth*, *122*(5), 3392–3409. https://doi.org/10.1002/2016JB013658

Neuzil, C. E. (1995). Abnormal pressures as hydrodynamic phenomena. *American Journal of Science*, *295*(6), 742–786. https://doi.org/10.2475/ajs.295.6.742

Niemeijer, A., Marone, C., & Elsworth, D. (2010). Frictional strength and strain weakening in simulated fault gouge: Competition between geometrical weakening and chemical strengthening. *Journal of Geophysical Research*, *115*(B10). https://doi.org/10.1029/2009JB000838

Peacock, S. M. (2009). Thermal and metamorphic environment of subduction zone episodic tremor and slip. *Journal of Geophysical Research*, *114*(B8). https://doi.org/10.1029/2008jb005978

Phillips, N. J., Motohashi, G., Ujiie, K., & Rowe, C. D. (2020). Evidence of localized failure along altered basaltic blocks in tectonic mélange at the updip limit of the seismogenic zone: Implications for the shallow slow earthquake source. *Geochemistry, Geophysics, Geosystems*, *21*(7), e2019GC008839. https://doi.org/10.1029/2019GC008839

Roscoe, K., & Burland, J. B. (1968). On the generalized stress-strain behaviour of wet clay.

Rubin, A. M. (2008). Episodic slow slip events and rate-and-state friction. *Journal of Geophysical Research*, *113*(B11). https://doi.org/10.1029/2008JB005642

Ruina, A. (1983). Slip instability and state variable friction laws. *Journal of Geophysical Research*, *88*(B12), 10359–10370. https://doi.org/10.1029/jb088ib12p10359

Saffer, D. M., & Tobin, H. J. (2011). Hydrogeology and mechanics of subduction zone forearcs: Fluid flow and pore pressure. *Annual Review of Earth and Planetary Sciences*, *39*(1), 157–186. https://doi.org/10.1146/annurev-earth-040610-133408

Saffer, D. M., & Wallace, L. M. (2015). The frictional, hydrologic, metamorphic and thermal habitat of shallow slow earthquakes. *Nature Geoscience*, *8*(8), 594–600. https://doi.org/10.1038/ngeo2490

Scholz, C. H. (1998). Earthquakes and friction laws. *Nature*, *391*(6662), 37–42. https://doi.org/10.1038/34097

Scruggs, V. J. (1997). *Frictional constitutive properties and related microstructures of albite, muscovite, biotite and talc*. Brown University.

Scuderi, M. M., & Collettini, C. (2016). The role of fluid pressure in induced vs. triggered seismicity: Insights from rock deformation experiments on carbonates. *Scientific Reports*, *6*(1), 24852. https://doi.org/10.1038/srep24852

Scuderi, M. M., Collettini, C., & Marone, C. (2017). Frictional stability and earthquake triggering during fluid pressure stimulation of an experimental fault. *Earth and Planetary Science Letters*, *477*, 84–96. https://doi.org/10.1016/j.epsl.2017.08.009

Segall, P., Rubin, A. M., Bradley, A. M., & Rice, J. R. (2010). Dilatant strengthening as a mechanism for slow slip events. *Journal of Geophysical Research*, *115*(B12). https://doi.org/10.1029/2010JB007449

Shelly, D. R., Beroza, G. C., Ide, S., & Nakamula, S. (2006). Low-frequency earthquakes in Shikoku, Japan, and their relationship to episodic tremor and slip. *Nature*, *442*(7099), 188–191. https://doi.org/10.1038/nature04931

Shibazaki, B., & Iio, Y. (2003). On the physical mechanism of silent slip events along the deeper part of the seismogenic zone. *Geophysical Research Letters*, *30*(9). https://doi.org/10.1029/2003GL017047

Shibazaki, B., & Shimamoto, T. (2007). Modelling of short-interval silent slip events in deeper subduction interfaces considering the frictional properties at the unstable—Stable transition regime. *Geophysical Journal International*, *171*(1), 191–205. https://doi.org/10.1111/j.1365-246X.2007.03434.x

Sibson, R. H., Robert, F., & Poulsen, K. H. (1988). High-angle reverse faults, fluid-pressure cycling, and mesothermal gold-quartz deposits. *Geology*, *16*(6), 551–555. https://doi.org/10.1130/0091-7613(1988)016<0551:harffp>2.3.co;2

Skarbek, R. M., Rempel, A. W., & Schmidt, D. A. (2012). Geologic heterogeneity can produce aseismic slip transients. *Geophysical Research Letters*, *39*(21). https://doi.org/10.1029/2012GL053762

Skarbek, R. M., & Savage, H. M. (2019). RSFit3000: A MATLAB GUI-based program for determining rate and state frictional parameters from experimental data. *Geosphere*, *15*(5), 1665–1676. https://doi.org/10.1130/ges02122.1

Sleep, N. H., & Blanpied, M. L. (1992). Creep, compaction and the weak rheology of major faults. *Nature*, *359*(6397), 687–692. https://doi.org/10.1038/359687a0

Tembe, S., Lockner, D. A., & Wong, T.-F. (2010). Effect of clay content and mineralogy on frictional sliding behavior of simulated gouges: Binary and ternary mixtures of quartz, illite, and montmorillonite. *Journal of Geophysical Research*, *115*(B3). https://doi.org/10.1029/2009jb006383

Thomas, A. M., Beroza, G. C., & Shelly, D. R. (2016). Constraints on the source parameters of low-frequency earthquakes on the San Andreas Fault. *Geophysical Research Letters*, *43*(4), 1464–1471. https://doi.org/10.1002/2015GL067173

Ujiie, K., Saishu, H., Fagereng, Å., Nishiyama, N., Otsubo, M., Masuyama, H., & Kagi, H. (2018). An explanation of episodic tremor and slow slip constrained by crack-seal veins and viscous shear in subduction mélange. *Geophysical Research Letters*, *45*(11), 5371–5379. https://doi.org/10.1029/2018GL078374

Van Diggelen, E. W. E., De Bresser, J. H. P., Peach, C. J., & Spiers, C. J. (2010). High shear strain behaviour of synthetic muscovite fault gouges under hydrothermal conditions. *Journal of Structural Geology*, *32*(11), 1685–1700. https://doi.org/10.1016/j.jsg.2009.08.020

Watson, J. T. R., Basu, R. S., & Sengers, J. V. (1980). An improved representative equation for the dynamic viscosity of water substance. *Journal of Physical and Chemical Reference Data*, *9*(4), 1255–1290. https://doi.org/10.1063/1.555631

Wibberley, C. A. (2002). Hydraulic diffusivity of fault gouge zones and implications for thermal pressurization during seismic slip. *Earth Planets and Space*, *54*(11), 1153–1171. https://doi.org/10.1186/bf03353317

Wood, D. M. (1990). *Soil behaviour and critical state soil mechanics*. Cambridge university press.

Xing, T., Zhu, W., French, M., & Belzer, B. (2019). Stabilizing effect of high pore fluid pressure on slip behaviors of gouge-bearing faults. *Journal of Geophysical Research: Solid Earth*, *124*(9), 9526–9545. https://doi.org/10.1029/2019jb018002